ISSN 0377-9416

PMAI

Volume 31, December 2005

TRANSACTIONS OF POWDER METALLURGY ASSOCIATION OF INDIA

Editor - P. Ramakrishnan

PMAI

Powder Metallurgy Association of India

TRANSACTIONS OF POWDER METALLURGY ASSOCIATION OF INDIA

Vol. 31, December 2005

Editor

P.Ramakrishnan

Editorial

The 31st Annual Technical Meeting of Powder Metallurgy Association of India was held along with the International conference with Trade Exhibition on Particulate Materials for Automotive and Engineering Industry during Feb.3-6, 2005 at Renaissance Mumbai Hotel and Convention Center, Mumbai. The proceedings of the International Conference will be published soon.

The highlights of the Annual Technical Meeting include the Dr. R.V.Tamankar Memorial lecture delivered by Shri.Bijoy Sarma and Shri.P.R.Roy Memorial lecture by Dr.V.N.Vaidhya. Dr.G.S.Tendolkar Award for the best paper was shared by Bharati R.Rehani and P.R.Joshi of M.S.University, Baroda; and Anil Borah, P.S.Robi, A.Srinivasan and Ajit L.Mujamdar of I.I.T., Guwahati. A multilevel (2 from top and 3 from bottom) oil pump flange-iron, nickel, moly steel; developed by GKN Sinter Metals (of the Fiat, General Motor power train project for the Suzuki's 1.3 D Engine) was adjudged as the best PM product. Selected papers presented at the ATM along with the award winning papers are included in this 31St volume of the Transaction of PMAI.

We acknowledge the excellent work done by the past President Dr.T.R.Rama Mohan, Secretary Shri. U.Basak, Treasurer Shri.P.V.Hegde along with other office bearers and welcome our new President Shri. D.K.Varshney, Secretary Shri.Bijoy Sarma, Treasurer Dr.V.Chandrasekaran along with other members of office bearers.

PMAI wishes its readers a very happy and prosperous New Year-2006

P.Ramakrishnan

Presidential Address

At the outset I congratulate all the participating members, present and past office bearers on successfully completion of 32 years and making PMAI a forceful and effective body in Indian P/M horizon.

To meet the challenges of globalization we need to create intense interaction between P/M manufacturers, research organizations, equipment suppliers, raw material manufacturers and academic institutions. We should mobilize their strength to achieve cost effectiveness while maintaining quality of products and services at par with international standards.

Indian organizations with international presence like CII can be induced to promote the cause of the Indian P/M Industry.

We also have to make efforts to affiliate PMAI with national and international bodies like APMI, ASTM, MPIF etc. we should achieve this objective by 2007.

Presently all elected office bearers are located in different parts on the country and interaction is not easy. I propose that we should have a permanent secretariat located in a suitable place which will serve as the head quarters of PMAI. It should have a permanent staff, library and other infrastructure to effectively manage the workings. This will effectively reduce the load on office bearers and help in maintaining continuity and upkeep of proper records.

Let the acronym of PMAI also mean PROFESIONALLY MANAGED APEX INSTITUTION.

D.K. Varshney
President, PMAI

TRANSACTIONS OF
POWDER METALLURGY ASSOCIATION OF INDIA

Vol. 31, December 2005

CONTENTS

1] **PROCESSING AND CHARACTERIZATION OF RUTHENIUM ALUMINIDE ALLOYS BY POWDER METALLURGY AND SOLIDIFICATION TECHNIQUES**
Anil Borah, P.S. Robi, A. Srinivasan, Ajit L. Mujumdar 01

2] **SILVER-GRAPHITE NANOCOMPOSITE MATERIALS FOR ELECTRICAL CONTACT APPLICATIONS**
Bharati.R.Rehani and P.B.Joshi 07

3] **MICROWAVE LIQUID PHASE SINTERING OF Co-Cu ALLOYS**
P. Garg and A. Upadhyaya 11

4] **Cu-Co-Fe PRE-ALLOYED POWDER AS A MATRIX MATERIAL FOR DIAMOND TOOOLS**
R. R. Thorat, P. K. Brahmankar and T. R. R. Mohan 17

5] **INJECTION MOULDING OF STAINLESS STEEL POWDERS**
Aebgin John Poickattil and T.R.Rama Mohan 21

6] **SYNTHESIS OF PMN-PT CERAMICS FROM $M_g Nb_2 O_6$ PRECURSOR**
SUJAL UPADHYAY, T. R. RAMA MOHAN 26

7] **STRENGTHENING BRASS POWDER COMPONENTS**
Akhter H. Ansari 31

8] **POLYMETHYLMETHACRYLATE / HYDROXYAPATITE COMPOSITES**
Rajalaxmi Dash, Deepak K. Pattanayak, B. T. Rao, R. C. Prasad and T. R. Rama Mohan 35

9] **NANOSTRUCTURED IRON POWDER BY CARBOTHERMIC REDUCTION OF MECHANICALLY ACTIVATED MILL SCALE**
Manoj Dubey, Ashish Bhatnagar, N. Charles, Nilima Lodha, P.R. Soni 42

PROCESSING AND CHARACTERIZATION OF RUTHENIUM ALUMINIDE ALLOYS BY POWDER METALLURGY AND SOLIDIFICATION TECHNIQUES

Anil Borah, P.S. Robi, A. Srinivasan#, Ajit L. Mujumdar

Department of Mechanical Engineering, #Department of physics
Indian Institute of Technology Guwahati, India 781039.

ABSTRACT

RuAl alloys exhibit a combination of properties like high melting point (≈ 2050 °C), high strength at room and elevated temperatures, high resistance to environmental corrosion in some very severe chemical media as well as useful room temperature ductility and toughness. In spite of these promising properties, the processing of ruthenium aluminide still remains a challenge. Powder metallurgy (P/M) technique is a viable method of processing these alloys so as to circumvent these drawbacks. The present paper discusses the processing of binary RuAl alloys and ternary Ru-Al-Ni alloys by P/M as well as solidification technique. The extent of mechanical alloying during attrition milling is characterized by X-ray diffractometer (XRD). The final microstructure obtained for these alloys processed by P/M technique is compared with that obtained by casting technique. Dense pellets with homogeneous structure were obtained for the P/M processed alloys after sintering. The cast and heat treated alloys showed segregation and non-homogeneous structure with a high amount of porosities. It is concluded that P/M technique is a better processing route compared to the solidification technique.

1. INTRODUCTION

Intermetallic materials like nickel and titanium aluminides are characterized by high elevated temperature strength, high oxidation and corrosion resistance, and high melting point. However, their applications for structural use are impeded due to their poor room temperature ductility and toughness. Recent studies revealed that intermetallic ruthenium aluminide (RuAl) alloys exhibit the unusual combination of very high melting point (≈ 2050 °C), high strength at room and elevated temperatures, high resistance to environmental corrosion in some very severe chemical media, as well as useful room temperature ductility and toughness [1-5]. Though the properties obtained for ruthenium aluminide are promising for high temperature structural applications, the processing of these materials still remains a challenge. The high thermodynamic stability of RuAl imposes a number of restrictions for processing these alloys by conventional solidification routes [4-5]. Most of the refractory crucible linings tend to get attacked by the high temperature melt. Aluminum vaporizes at temperature above 1900 °C leading to high chemical inhomogeneity, deviation from the stoichiometric composition and porous material during casting. RuAl alloys can be processed by powder metallurgy (P/M) techniques and have the following advantages over the casting technique [6] (i) The ruthenium source material is converted directly from the powder, which is the primary product of the refining process. (ii) The intrinsic enthalpy of reaction is the thermally efficient driving force for densification, circumventing the high furnace temperatures necessary for melting or sintering. (iii) The material can be processed at low (sintering) temperatures, whereby volatilization of aluminum is prevented, resulting in a chemically homogeneous and porosity free material. (iv) The technique has the unique advantage of successfully processing several alloys and compounds, which cannot be prepared by conventional melt techniques, especially in systems containing elements with remarkably different melting points. (v) The material processed by P/M technique is free of coring and segregation which are observed in the products produced by melting technique. (vi) Grain size distribution is narrow in materials prepared by P/M route. (viii) Near net shaped components can be obtained ensuring minimum material wastage and circumventing the need of machining process.

Mechanical alloying process is a method for producing composite metal powders with controlled fine microstructure. This can be achieved by milling elemental powders necessary for the formation of the alloy under controlled atmosphere in an attrition mill. For proper mechanical alloying, it is essential to have minimum two types of powders viz. one ductile material and the other

brittle material. In an attrition mill, due to the very high energy impact of the powder mixtures and hard balls, the ductile powder undergoes plastic deformation resulting in extensive work hardening. The brittle powder fragments into a fine powder and gets embedded into the ductile phase. The hardened ductile powders are repeatedly cold welded, fractured and re-welded leading to mechanical alloying [7]. It is imperative to strike a balance between the cold welding and fracturing processes in order to achieve efficient mechanical alloying. Attempts aimed on producing mechanically alloyed RuAl alloy powders have been reported in the literature [8–10]. Attempts were also carried out to characterize the structure of RuAl alloys processed by solidification techniques [1, 3-4, 11].

The high cost of ruthenium severely limits the use of these materials in structural applications. However, these can be used as a high temperature coating material for various applications such as turbine blades and shafts. One method of reducing the cost of these materials is by substituting ruthenium with elements like nickel, cobalt, etc. The mechanical properties of the material depend on the microstructure obtained and are having a strong influence on the processing route adopted. For justification of use of these materials in the above applications, a systematic processing followed by characterization of structure and properties is required. A comparison of the microstructure obtained for the RuAl alloys processed by different techniques is, therefore necessary. The present paper discusses the processing of binary RuAl alloys and ternary Ru-Al-Ni alloys by P/M as well as solidification technique. The extent of mechanical alloying during attrition milling is characterized by XRD and discussed. The final microstructure obtained for these alloys processed by P/M technique consisting of attrition milling, cold compaction followed by sintering is compared with that obtained by arc melting technique.

2. EXPERIMENTAL PROCEDURES

Elemental powders of Ru (purity of 99.4%, average size 4μm), Al (purity of 99.9%, average size 7 μm) and Nickel with (purity of 99% and size ~ 10 μm) were used as the starting materials. The processing of the materials was carried out by two techniques: (i) powder metallurgy technique, and (ii) solidification route. The elemental powders of stoichiometric compositions $Ru_{47}Al_{53}$, and $Ru_{38.5}Al_{16.5}Ni_{45}$ were used as the starting material.

Powder metallurgy processing was carried out by milling the elemental powders for 50 hours in an attrition mill using 1 wt% stearic acid ($C_{18}H_{36}O_2$) as the process control agent. Milled powders were taken out at regular time intervals and the structural analysis of the milled powder was carried out by XRD, using Cu $K\alpha$ radiation (λ = 1.54°A) on SEIFORT XRD 3002 PJ/T powder X-ray diffractometer. The extent of alloying was monitored from the relative intensities of the different peaks from the XRD data. X-ray peak profile from a single reflection could be approximated to a Lorentzian curve. Multiple (upto 3) Lorentzians were used for analyzing overlapping peaks. From the peak broadening data the particle sizes and strain of Ru, RuAl and Ni phases present in the as-milled powder samples were estimated from the full width at half maximum (FWHM) of the respective XRD peaks using the Williamson-Hall method [12]. This was followed by degassing, cold compaction of the milled powders at a pressure of 500 MPa to obtain 10 mm diameter X 10 mm height pellets, and then sintering at 1500 °C for 24 hours. The details regarding the extent of mechanical alloying and the compaction procedure are explained elsewhere [8].

For processing by solidification route, the powders were mixed homogeneously in a mortar and pestle. To avoid the loose powder from flying off during the arc melting, the powder mixture was compacted at a pressure of 200 MPa in a die and punch assembly to obtain a cold compact rectangular rod of size 50mm X 12mm X 10mm. This was kept in the water cooled copper mold of a laboratory level arc furnace and evacuated to a pressure of 10^{-5} mbar. This was followed by purging with argon gas. Melting was done by striking the arc between the tungsten electrode and the cold compacted alloy. The arc was struck 2-3 times along the length of the sample to ensure proper melting of the entire rod. The arc was stopped and the sample was allowed to solidify in the water cooled copper furnace hearth. A part of the solidified alloy rod was annealed at 1400 °C for 24 hours in an argon atmosphere to study the structural evolution taking place during the heat treatment.

The cast samples, cast and heat treated samples as well as the powder metallurgy processed samples were sliced using a precision saw and polished for microscopic observation following the standard metallographic specimen preparation techniques. The microstructure of the samples were studied using a Leo make 1430 VP model scanning electron microscope (SEM) attached with OXFORD energy dispersive X-ray analysis (EDS) system.

3. RESULTS AND DISCUSSION

Fig 1 (a) & (b) shows the XRD patterns of milled powders of stoichiometric composition $Ru_{47}Al_{53}$ and $Ru_{38.5}Al_{16.5}Ni_{45}$ respectively. In the powders with $Ru_{47}Al_{53}$, no evidence of formation of RuAl phase was found up to 2 hours of milling. Peaks corresponding to Al were not seen after two hours of milling. Peaks corresponding to RuAl phase were observed after 7 hours of milling indicating the mechanical alloying. With further milling, peak broadening was observed for Ru and RuAl phases indicating a

continuous size reduction and presence of residual stress in the milled powders. A detailed analysis of the size reduction and residual stresses in this material is reported elsewhere [8].

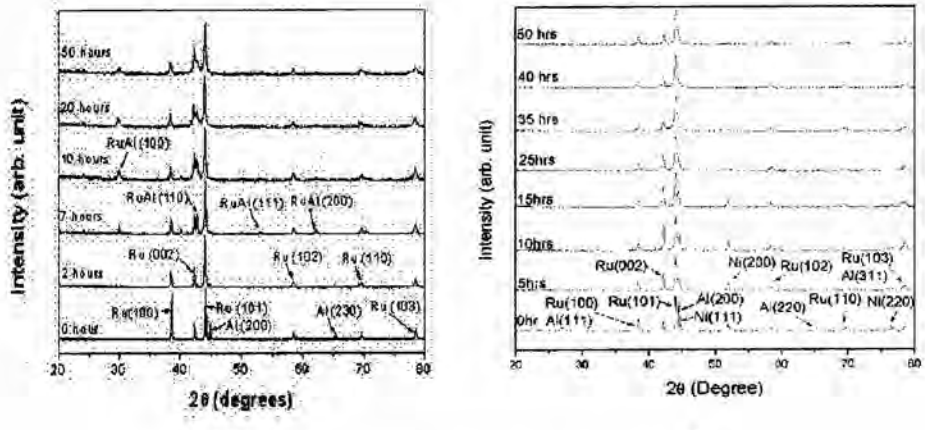

(a) (b)

Fig 1. XRD pattern at various milling times for (a) $Ru_{47}Al_{53}$ and (b) $Ru_{38.5}Al_{16.5}Ni_{45}$

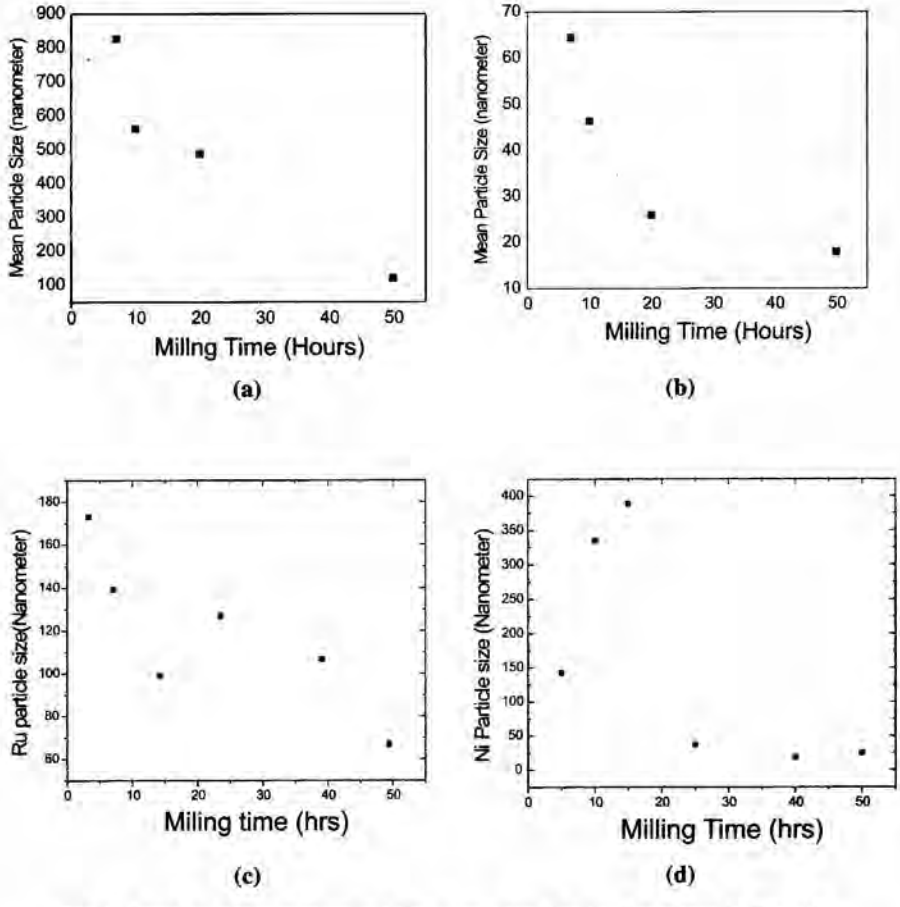

Fig 2. Particle size variation with milling time for (a) Ru phase in $Ru_{47}Al_{53}$, (b) RuAl phase in $Ru_{47}Al_{53}$, (c) Ru in $Ru_{39.5}Al_{16.5}Ni_{45}$, and (d) Ni phase in $Ru_{39.5}Al_{16.5}Ni_{45}$

Fig 1(b) shows XRD pattern for $Ru_{39.5}Al_{16.5}Ni_{45}$ system and does not reveal the formation of any binary or ternary phases during the milling process. Intensity of Al peaks disappeared after 5 hours of milling. Chakravorty and West [13] have reported that the continuous solid solution across the Ru-Al-Ni pseudo-binary range was interrupted by a miscibility gap. They proposed a constitutional diagram for Ru-Al-Ni system consisting of an extensive three phase field of β-RuAl, Ru solid solution and Ni solid solution (γ). The disappearance of the Al peaks with milling time might be an indication of the formation of a disordered γ-phase and Ru solid solution formation during the milling process.

Analysis of various peaks from the XRD data revealed continuous reduction in the powder size with milling time. Fig 2 shows the results of the crystallite sizes for various phases with milling time for the above compositions of the powder mixture. The sizes of Ru and RuAl in $Ru_{47}Al_{53}$ system were 120 nm and 17 nm respectively and that of Ru and Ni in $Ru_{39.5}Al_{16.5}Ni_{45}$ system were 66 nm and 25 nm respectively after 50 hours of milling. The variation of Ru particle size with respect to the milling time is expected due to the brittle nature of Ru. However, Ni particle size increases initially up to 15 hours of milling time, thereafter decreasing rapidly.

SEM images of milled, cold compacted and sintered $Ru_{47}Al_{53}$ and $Ru_{39.5}Al_{16.5}Ni_{45}$ alloys are shown in Fig 3. No evidence of porosities was found in these sintered samples. The alloy with composition $Ru_{47}Al_{53}$ revealed the presence of a uniform distribution of grey RuAl phase (identified as $Ru_{56}Al_{44}$) and white ruthenium rich phase (identified as $Ru_{95}Al_5$) in a highly Al enriched matrix. The grain sizes of these phases (grey and white) were found to be less than 5 μm. Microstructure of sintered $Ru_{39.5}Al_{16.5}Ni_{45}$ alloy, shown in Fig 3(b), revealed a uniform distribution of a white phase (identified as $Ru_{67}Ni_{33}$) and a black phase (identified as $Ru_3Al_{61}Ni_{34}Fe_2$).

Alloys in the as-cast condition, revealed the presence of large amount of gas porosities as well as micro-porosities. The gas porosities observed is due to the vaporization of aluminum due to the high temperature during the melting stage. The analysis of the alloy with a starting composition of $Ru_{47}Al_{53}$ revealed aluminum loss which might have occurred during the melting stage. The structure of this alloy shown in Fig 4 revealed a continuous network of eutectic mixture ($Ru_{88}Al_{12}$ + $Ru_{63}Al_{37}$) around the pro-eutectic ($Ru_{56}Al_{44}$) phase. The microstructure of the cast alloy after heat treatment is shown in Fig 5. Fine needle shaped second phase precipitates were observed in the pro-eutectic RuAl phase. From this observation as well as from the binary phase diagram [14], it can be concluded that this alloy exhibits precipitation hardenable behavior.

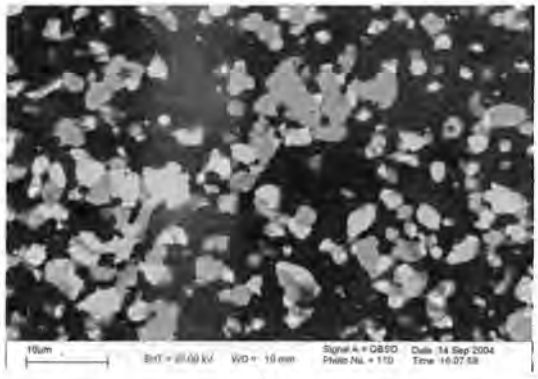

(a)

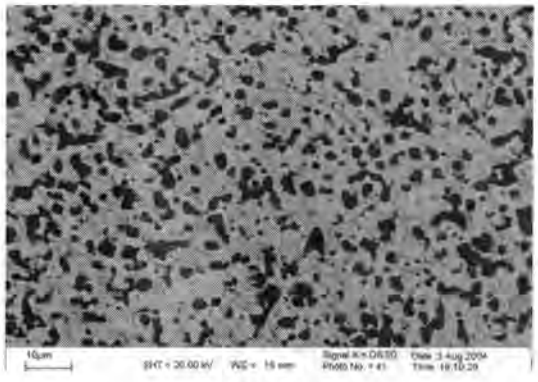

(b)

Fig 3: SEM images of sintered (a) $Ru_{47}Al_{53}$, and (b) $Ru_{39.5}Al_{16.5}Ni_{45}$

(a)

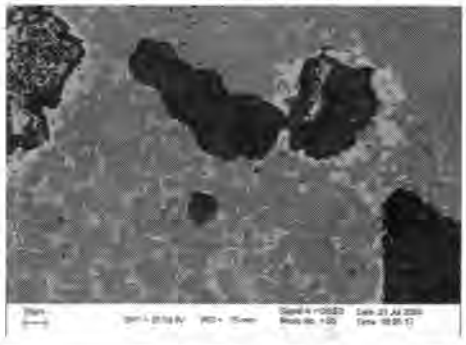

(b)

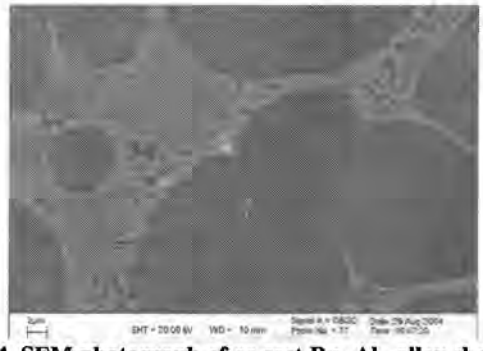

Fig 4. SEM photograph of as cast $Ru_{47}Al_{53}$ alloy showing (a) porosities, and (b) micro-structure.

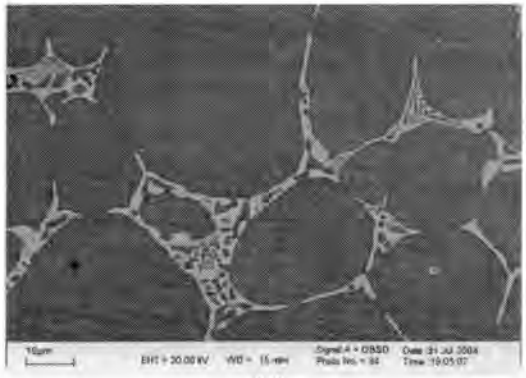

(a)

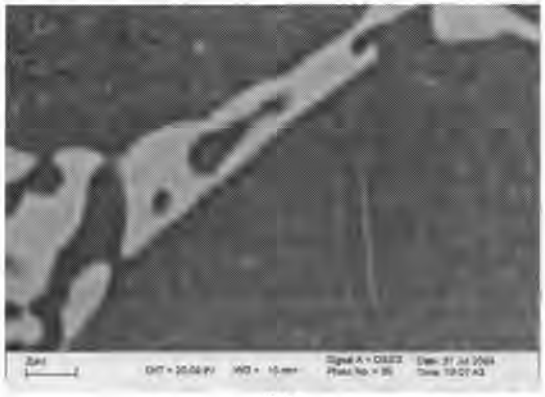

(b)

Fig-5: SEM photograph of as-cast and heat treated $Ru_{47}Al_{53}$ alloy showing presence of fine needle shape second phase precipitates (a) at low magnification and (b) at high magnification.

SEM photograph of as-cast $Ru_{39.5}Al_{16.5}Ni_{45}$ alloy is shown in Fig 6(a). The cast structure revealed dendritic structure at low magnification. The micro-structure consists of two phases: a primary white phase (identified as $Ru_{66}Al_7Ni_{27}$) and a dark phase (identified as $Ru_{28}Al_{15}Ni_{57}$). Overall composition of the alloy was $Ru_{38}Al_{13}Ni_{48}$. The overall composition of the alloy showed a decrease in aluminium and increase nickel concentration. A structural evolution was found to occur when the cast alloy was annealed at 1400 °C for 24 hrs, shown in Fig 6 (b). During the annealing process, the morphology of both the phases changed to a laminar type structure. It appears that this morphological change occurring in these two phases is due to a diffusion assisted reaction. Due to the rapid cooling of the molten metal inside the water cooled copper mold, the solidification of the alloy occurs under a non equilibrium condition resulting in the two phases deviating from the equilibrium composition. During the annealing process, individual atoms diffuse to obtain equilibrium composition resulting in a laminar structure as shown Fig 6 (b). It has been proposed by researchers that the development of laminar structure can lead to the improvement in the ductility and toughness of intermetallic alloys [15].

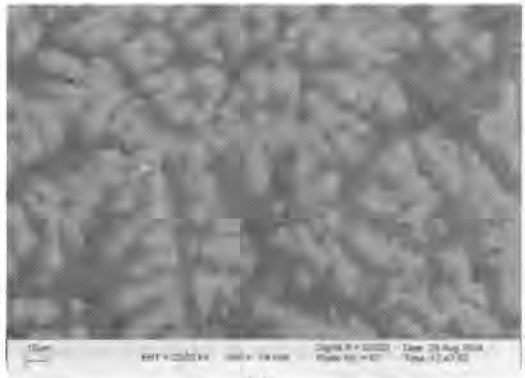

(a)

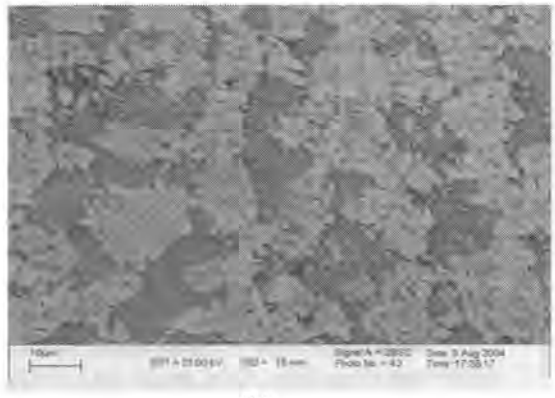

(b)

Fig 6. SEM micrographs of $Ru_{39.5}Al_{16.5}Ni_{45}$ alloy (a) in as-cast condition and (b) cast and annealed.

4. CONCLUSIONS

RuAl and Ru-Al-Ni alloys were prepared by two different routes, viz., solidification and P/M. Microstructural studies of the alloy prepared by casting revealed loss of aluminium due to volatilization resulting in gas porosities. Micro-porosities occurred due to shrinkage during solidification of the alloy. Microstructure of binary RuAl alloy consisted of primary dendrites of RuAl phase surrounded by a continuous network of eutectic lamellae. Heat treated cast samples showed a precipitation reaction resulting in needle shaped precipitates in the primary RuAl phase. Ternary Ru-Al-Ni alloy showed dendritic structure consisting of two phases, which resulted in a laminar type of structure during the annealing process.

The microstructure of RuAl processed by P/M route revealed a uniform distribution of fine ruthenium rich and aluminium rich phases in the matrix. Sintered alloys with 97% of the theoretical density devoid of porosities were obtained. Absence of a eutectic network structure, very fine grain size, and uniform distribution of phases are the advantages of the P/M processed alloy. These observations suggest that the P/M processing of RuAl alloys is superior compared to the solidification technique.

ACKNOWLEDGEMENTS

The authors acknowledge Indian Space Research organization (ISRO) for the funding of this work as per the sanction No. 9/1/(1)/99-II. The authors also thank Mr. K. Susheelan Nair, Vikram Sarabai Space Centre, Thiruvananthapuran, India, for his valuable suggestions and technical support during the course of this project.

REFERENCES

[1] R.L. Fleischer, R.D. Field and C.L. Briant, Mechanical properties of high temperature alloys of RuAl, *Met. Trans. A*, Vol. 22A, pp 404-414, (1991)

[2] R.L. Fleischer and McKee D.W., Mechanical and oxidation properties of RuAl based high temperature alloys, *Met. Trans. A*, Vol. 24A, pp 769-763, (1993).

[3] I.M. Wolff and G. Sauthoff, Mechanical properties of Ru-Ni-Al alloys, *Metall. Mater. Trans.* A, Vol. 27A, pp 1395-1400, (1996).

[4] I.M. Wolff and G. Sauthoff, Role of intergranular phase in RuAl with substitutional additions, *Acta Mater.*, Vol. 45(7), pp 2949-2969, (1997)

[5] I.M. Wolff, Towards a better understanding of ruthenium aluminide, *JOM*, pp 34-39, (1997).

[6] I.M. Wolff, Synthesis of RuAl by reactive powder processing, *Metall. Mater. Trans., A*, Vol. 27A, pp 3688-3699, (1995).

[7] L.Lu and M.O.Lai, *Mechanical Alloying*, Kluwer Academics, Boston, (1998).

[8] Anil Bora et. al., Powder metallurgy processing of ruthenium aluminium alloys, *J. Material Processing Technology*, Vol. 153–154, pp 952–957, (2004).

[9] K.W. Liu and F. Mucklich, Thermal stability of nano-RuAl produced by mechanical alloying, *Acta Mater.*, Vol. 49, pp 395-403, (2001).

[10] K.W. Liu and F. Mücklich High-temperature stability of nano-grained B2-structured RuAl-based intermetallics by mechanical alloying, *Intermetallics*, In Press, Available online, (2004).

[11] N. Ilic' et.al., Properties of eutectic Ru–Al alloy produced by ingot metallurgy, *Materials Science and Engineering A*, Vol. 329-331, pp 38–44, (2002).

[12] Yu. Rosenberg, V. Sh Machavariani, A Voronel, S Garber, A Rubshtein, A I Frenkel and E A Stern, Strain energy density in the X-ray powder diffraction from mixed crystals and alloys, *J. Phys.: Condens. Matter*, Vol. 12, pp 8081-8088, (2000).

[13] S. Chakravorty and D.R.F. West, The constitution of the Ni-Al-Ru System, *J. Mater. Sci.*, Vol. 21, pp 2721-2730, (1986).

[14] T. B. Massalski (ed.), *Binary Alloy Phase Diagrams*, ASM International, USA, 2nd edition, pp 204, (1990).

[15] I.M. Wolff and G. Sauthoff, High-Temperature behavior of precious metal base composites, *Metall. Trans.*, Vol. 22A, pp 2642-2652, (1996).

SILVER-GRAPHITE NANOCOMPOSITE MATERIALS FOR ELECTRICAL CONTACT APPLICATIONS

Bharati.R.Rehani and P.B.Joshi

Dept. of Metallurgical Engineering, M. S. University of Baroda, Baroda-390 001, India

ABSTRACT

Silver-base composites are developed as electrical contact materials for switchgear applications in devices such as contactors, relays, circuit breakers, switches, etc. owing to their low arc erosion, improved antiwelding properties and lower contact resistance compared to contacts made from pure metals and alloys. Silver-graphite composites with graphite percentage in the range of 0.25 wt. percent to about 50 wt. percent find applications as *make and break* type switching contacts and slip ring / sliding contacts in switchgear devices. Ag-C contacts are currently manufactured by conventional powder metallurgy route involving blending or milling of elemental silver and graphite powder particles followed by their consolidation, sintering and extrusion to bulk solids. However, large difference in the bulk density of these two constituent materials leads to segregation during milling and eventually heterogeneous microstructure responsible for inferior electrical contact properties.

The present work deals with synthesis of silver-graphite nanocomposite powders (with 1 to 5 wt. percent graphite) by mechanical alloying in a high-energy attritor followed by their pressing – sintering - repressing into bulk solids. The compacts so produced are found to exhibit density and electrical conductivity values comparable to those of conventionally produced materials, whereas they offer improved microstructure in terms of dispersion of graphite in silver matrix. The silver-graphite contacts so produced from mechanically alloyed Ag-C nanocomposite powders are expected to offer superior electrical contact properties viz. greater resistance to arc erosion and lower tendency to contact welding as well as low contact resistance.

INTRODUCTION:

The silver-graphite composites are widely used as switchgear contacts for commercial as well as industrial applications. The low- graphite grades (containing less than 10-15 wt.% graphite) are used as *make and break* type switching contacts whereas high-graphite grades (containing more than 15 wt.% graphite) find applications as sliding contacts in electrical brushes.

The silver-graphite contacts have low contact resistance, high conductivities, self-lubricating properties and anti-welding properties provided contact pressures are low [1]. Silver-graphite contacts are used for applications requiring rubbing speeds less than 0.03 meters per seconds and light pressures [2]. Low-graphite electrical contacts find applications as rheostats, contact brushes, contactors, molded case circuit breakers and as slip ring contacts, etc. [3].

The silver-graphite contacts are manufactured by using conventional powder metallurgy route of blending / milling of elemental silver and graphite powder particles, followed by their pressing, sintering and extrusion as ingot. The extruded ingot is further processed to form wrought silver-graphite strips or wires, which can subsequently be used to produce contact pieces. The Ag-C contacts are also produced by pressing, sintering and repressing of silver-graphite composite powders [3]. However, large difference in bulk density/ specific gravity of these two constituent materials give rise to the problem of segregation during blending / milling operation and eventually heterogeneous microstructure responsible for inferior physical, metallurgical, and electrical contact properties.

The present investigation has been concerned with a study involving processing and property evaluation of Ag-1wt.%C, Ag-3wt.%C and Ag-5wt.%C contact materials produced by mechanical alloying (MA) route.

Mechanical alloying was developed by J.S.Benjamin at the laboratories of INCO Alloys International in the late 1960's for production of oxide-dispersion strengthened

super alloys [4]. Later on MA process has been modified and adopted to produce a wide range of materials such as amorphous/nanocrystalline materials, intermetallic compounds, metal-matrix composites, solid-solution alloys, etc [5 - 8]. During MA of ductile-ductile system like Ag-C, the powder particles develop a composite layered structure in the early stages of milling. On further milling, the structure is gradually refined and homogenized through the mechanical kneading action that the powder charge is subjected to and also by the diffusion across composite layers. Finally, the composition of individual powder particles reaches the composition of the starting powder blend along with the high degree of dispersion between the constituent phases[5].

EXPERIMENTAL PROCEDURE:

Elemental silver powder of 99.9 % purity and 10 μm average particle size and graphite powder of 99.5 % purity were used as the starting materials. The stoicheometric amounts of silver-graphite (Ag-1%C, Ag-3%C, Ag-5%C) were mixed in cylindrical blender at 130 rpm for 30 min. The blended powders were then subjected to attrition milling in a Szegwari type attritor, having stainless steel vial of 200 cc capacity. AISI 52100 grade hardened steel balls of 6.3 mm dia. were used as grinding media. The milling was carried out at a ball to charge ratio of 20:1 and at 400 rpm speed of attrition. The powder samples were drawn at specific time intervals during the course of milling and were characterized by X-ray diffraction (XRD) and Scanning Electron Microscopy (SEM) to monitor the degree of mixing between silver and graphite and also to study the changes in the powder morphology with progressive milling. Figure 1 shows the variation in peak intensity (a.u.) for silver and graphite phase with respect to milling time (hrs) for Ag-3%C composite powders. A Philips Xpertpro X-ray diffractometer with solid state zirconium detector was used for X-ray diffraction analysis. The diffraction profiles were obtained using a Cu target at a scan speed of 3° per min. within the 2θ range of 0 to 70°. The shape morphology of powder particles was examined using Jeol JSM 5610 LV model of Scanning Electron Microscope. The SEM microphotographs for Ag-3%C as- blended and 4 hrs milled powder samples are given in Figure 2(a) and (b).

The synthesized powders of three different compositions (viz. Ag-1%C, Ag-3%C, Ag-5%C) were pressed to get the green compacts of 10mm dia.x 2mm height at 300 MPa pressure on a 100-ton capacity hydraulic press in single action die compaction mode. The green compacts were sintered at 900 °C for 60 min. in vacuum in a resistance-heating furnace at a heating rate of 6 °C per min. The sintered compacts were repressed at 700 MPa.

The bulk solid contact pieces were subjected to density, electrical conductivity and microstructural evaluation. For microstructural examination a ground and polished sample in unetched condition was used. The micro section was subjected to examination using SEM in BSE mode without any surface modification. Figure 2 (c) shows the SEM micrograph for Ag-3%C bulk solid sample.

RESULT AND DISCUSSION:

The plot for variation of peak intensity v/s milling time for attrition milled powder (Figure 1) clearly indicates that the peak intensity for silver as well as graphite phase gradually decreases with milling time. The drop in peak intensity is attributed to broadening of X-ray diffraction peaks due to reduction in crystallite size with progressive milling. It is apparent from this plot that the diffraction peaks corresponding to graphite broadened to such an extent that the peak height practically ceases to zero and disappears completely. This is indicative of a very fine level of dispersion of graphite within the silver particles.

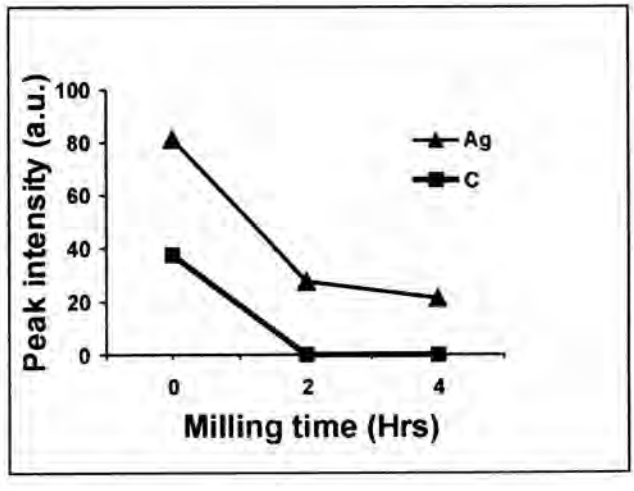

Fig. 1: Variation of peak intensity with respect to milling time for Ag – 3% C composite powders produced by MA

The SEM micrographs as shown in Figure 2(a) and 2 (b) for as- blended and milled powders, respectively clearly highlight the degree of dispersion of graphite in silver. The microphotographs also indicate the change in the shape morphology of Ag-C composite powder due to milling. The 4 hrs milled powder sample shows extensive flattening of silver particles along with fine and uniform dispersion of graphite within silver.

Table-1 gives a comparative data on properties of silver-graphite composite contacts developed under the investigation and those reported in the literature. The literature values are for silver-graphite contact materials

Fig 2(a): Ag-3%C as-blended powder showing heterogeneously dispersed grey coloured graphite particles in silver matrix

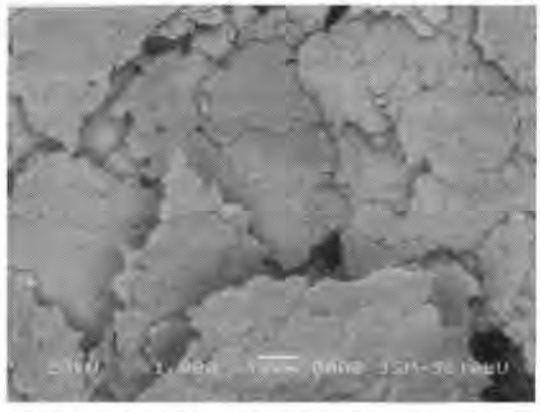

Fig 2(b): Ag-3%C attrition milled powder after 4 hrs of milling showing flattened silver particles and intimately dispersed grey graphite in silver

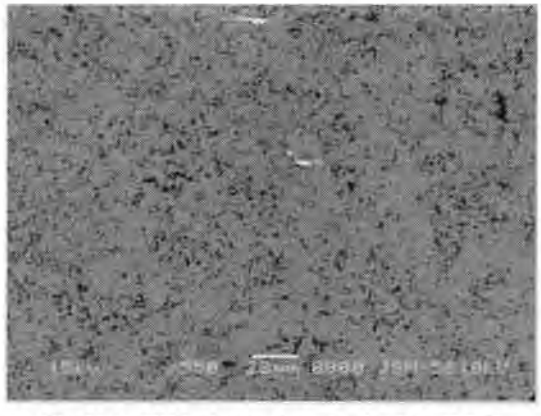

Fig 2(c): SEM photomicrograph of Ag-3%C sintered and repressed bulk solid contact material produced from attrition milled powder

produced by press-sinter-extrusion route using ball-milled powders. A critical comparison of the properties for the compacts produced under this investigation and the values reported in literature clearly indicates that it is possible to attain comparable levels of density and electrical conductivity in case of compacts produced from mechanically alloyed powders and subsequently processed by press-sinter-repress route.

TABLE: 1 Comparative Data on Properties of Ag-C Composite Contacts

Sr. No.	Composition	Property			
		Density g/cm³		Electrical conductivity (%IACS)	
		Measured value PSR	Literature value PSE	Measured value PSR	Literature value PSE
1	Ag-1%C	10.0	10.1	95	95
2	Ag-3%C	9.3	9.5	84	86
3	Ag-5%C	9.7	8.9	80	75

The point to be emphasized here is that the Ag-C contact materials produced from MA powders and processed by press-sinter-repress route give rise to a set of properties which are no way inferior to the properties obtained for Ag-C contact materials produced by press-sinter-extrude route. The process developed under this investigation thus claims to have an edge over the existing manufacturing practice for production of Ag-C contact materials.

REFERENCES:

1. H.H.Hausner, *Handbook of Powder Metallurgy*, Chemical Publishing Co. Inc., New York ,(1973), p.68.
2. R.H.T. Dixon and A.Clayton, *Powder Metallurgy for Engineers*, The Machinery Publishing Co.Ltd., London (1971).
3. P. G. Slade, Ed., *Electrical Contacts- Principles and Applications*, Marcel Dekkar Inc., New York (2002).
4. J.S. Benjamin, "Dispersion Strengthened Superalloys by Mechanical Alloying", *Met. Trans.*, Vol.1, October (1970), p.2943.
5. C.C.Koch, "The Synthesis and Structure of Nanocrystalline Materials Produced by Mechanical Attrition: A Review", *Nanostructured Materilas*, Vol.2, (1993), p.109.
6. B.S.Murty and S.Ranganathan, "Novel Materials-Synthesis by Mechanical Alloying/Milling", *International Materials Reviews*, Vol-43, No-3 (1998) p.101.
7. Li Lu and M.O.Lai," Formation of New Solid Materials in Solid State by Mechanical Alloying", *Materials and Design*, Vol.16, No.1,(1995),p.33.
8. G.B. Schaffer and P.G. McCormick, "Review on Mechanical Alloying", *Mat.Forum*, 16, (1992), p.91.

MICROWAVE LIQUID PHASE SINTERING OF Co-Cu ALLOYS

P. Garg and A. Upadhyaya

Department of Materials and Metallurgical Engineering
Indian Institute of Technology, Kanpur 208016, India

ABSTRACT

Over the recent years, there has been considerable interest in using microwave heating for sintering of metalic components. Despite its intrinsic advantages, the issue of shape control and microstructural segregation during microwave liquid phase sintering has not yet been adressed. The present study compares the effect of microwave and conventional heating on Co-Cu alloy compacts. In the present study Co-Cu alloys of varying compositions were microwave and conventionally sintered at 1200^0 C. The Co-Cu system forms a zero solid-liquid density difference system during liquid phase sintering and hence the gravity effects are expected to be non-existent. Sintered compacts were characterized for their sintered density, macrostructure and sterelogical parameters.

1. INTRODUCTION

The use of microwave sintering for synthesis of non metallic materials is wellestablished [1-4]. In conventional heating, heat transfer occurs from outside to inside. In microwave heating, heat is generated by the interaction of materials with microwave radiation, thus the material as such acts a source of energy, leading to uniform volumetric heating at a much higher rate than conventional heating. This results in faster and more uniform heating of the component, leading to finer microstructure and improved properties. Microwave heating also results in cost saving (reduced time and floor space) and is environmentally more clean.

However, microwave sintering of metallic systems was not considered for a long time, as metals tend to reflect microwaves. Recently, it was shown that microwave can couple with metals too, provided they are in a loose form rather than monolithic [5]. This has generated a great interest toward the fabrication of microwave sintered metallic P/M component, for production of component having improved properties than their conventionally sintered counterparts. Microwave sintering has been applied to a variety of metallic components - including iron and steels, aluminum, nickel, cobalt, copper and tin, and their alloys [6]. Ankelkar et al. [7] demonstrated higher sintered density, faster densification and higher hardness and flexural strength in microwave sintered Fe-2Cu-0.8C (FC0208) as compared to conventional sintering. Similar results were reported for Fe-Ni and Fe-Cu systems [5]. Upadhyaya et al. have studied the microwave sintering of premixed and prealloyed Cu-Sn [8] alloys. It was found that there is no compact swelling during microwave sintering of premixed Cu- 12Sn, whereas microwave supersolidus sintering of prealloyed Cu-12Sn results in a lower density than conventional sintering.

Although several studies have been, the basic mechanism for the microwave heating of metallic powders is still unclear. The advantages of microwave processing over conventional sintering are not clear. The results from the study on microwave sintering of Cu-12Sn alloy {8] indicates that the microwave sintering may be advantageous over conventional sintering in only certain cases. Moreover the issue of density induced solid-liquid segregation and distortion of compacts during microwave liquid phase sintering (LPS), especially when high liquid content may be present, has not been addressed in any of the studies. This poses a doubt as to whether the applicability of microwave processing is limited only to certain systems and over a limited range of compositions.

For the present study, the Cobalt-Copper system has been selected, as it provides a unique opportunity to look at a system that has a zero liquid–solid density difference. Thus any gravitational effects are expected to be nonexistent. This gives us an opportunity to study the microstructural and macrostructural evolution during microwave LPS in absence of gravitational effects. A previous study has reported the trends in the microstructural and macrostructural evolution during conventional LPS of Co-Cu alloy [9]. This study revealed the phenomenon of random flow of the liquid leading to formation of macropores at high liquid content. In the present study, Co-Cu alloys of varying compositions were microwave sintered at 1200°C. The sintered compacts were characterized for their microstructure features as well as macrostructural

distortion. The results were compared with those of the previous studies to highlight the differences in microstructural and macrosegregation evolution during microwave and conventional sintering, as well as to investigate any advantage offered by microwave sintering over conventional sintering in this particular system.

2. EXPERIMENTAL PROCEDURE

For the present study, Co-Cu system has been selected. Four alloy mixtures with varying Cu content (10, 20, 30 and 40 wt.%) were prepared by premixing the elemental powders. Fig. 1 shows the Co-Cu phase diagram and the alloy compositions used in the study. The copper powder was supplied by ACu Powder International and had a d50 of 14.10 μm. The cobalt powder was supplied by Kennametal Widia (India) Ltd, Bangalore and had a d50 of 11.0 μm. The mixtures were mixed in a turbula mixer for 30 minutes to achieve homogeneity.

The mixed powders were uniaxially die pressed at approximately 200 MPa using hydraulic press (Model CTM 50) of 50-ton capacity, to prepare cylindrical compacts 12.8 mm in diameter and approximately 3.5 mm in height. Zinc stearate was used as a die-wall lubricant to increase the flowability of powders and also for easy extraction of compacts.

The as pressed compacts were sintered in a 1 kW commercial microwave oven (Sinterwave, BHEL Corporate R&D, Hyderabad, India) with a 2.45 GHz multi-mold cavity in H2 atmosphere. The Compacts were sintered at 1200°C. Sintering was done for 30 min as microwave sintering generally leads to faster densification than conventional sintering. A high-density alumina tube of 71mm diameter and 670 mm length was positioned at the center of the oven by drilling holes on the side faces, with ends projecting outwards on both sides. An insulation package made of FibrefraxTM boards was used to surround the tubes at the center of the cavity to prevent heat dissipation. An infrared pyrometer (Mikron M680) was used to monitor the sample temperature. The pyrometer was coupled with data acquisition and display software on a personal computer.

The sintered samples were characterized for density and densification using dimensional measurements. The distortion was quantified by point-to-point measurement of the sectional diameter at various heights. For microstructural analysis, the samples were sectioned, mounted and polished using standard metallographic techniques. Microstructural analysis was done using Leica optical microscope with digital image acquisition capability. Subsequently, microstructures were stereologically quantified using image analyzer (Leica mikroscopie & system, GmbH, Wetzlar, Germany). The two-dimensional grain coordination number (Cc), grain contiguity (Cg), dihedral angle (Ô), and fraction solid content (Vs) were calculated manually with the help of image analyzer.

The Cg, which is microstructural measure of the relative interface area of solid-solid bonds versus the total interface area during liquid phase sintering, was calculated by Equation 1

$$C_g = \frac{2N_{ss}}{2N_{ss} + N_{sl}} \quad \text{..... (1)}$$

where NSS and NSL are the number of tungsten-tungsten contacts and tungstenmatrix contacts respectively per unit length of any given intercept. Connectivity or the two-dimensional coordination number (Cc) is two number of grains in contact with a central grain and the dihedral angle (Ô) is the angle formed by grain boundary with liquid during sintering. 200 values of each Ô and Cc were measured on a micrograph.

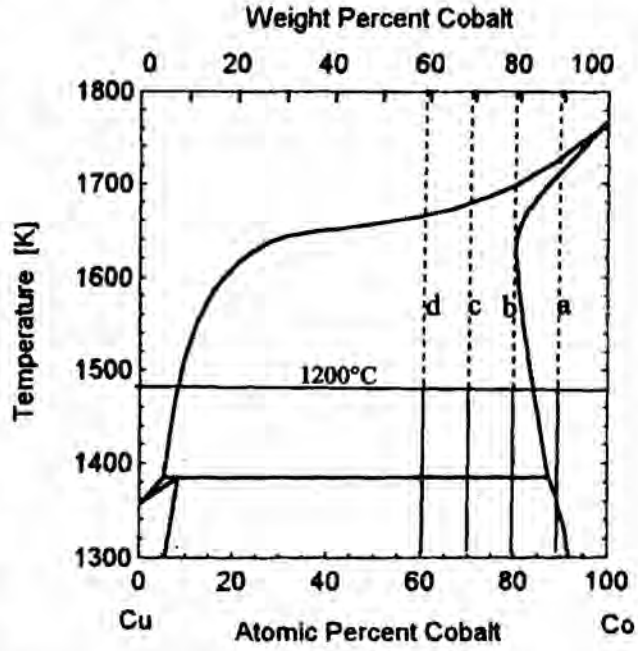

Sample	Composition	Liquid fraction @ 1200° C*
a	Co-10%Cu	0
b	Co-20%Cu	4%
c	Co-30%Cu	17%
d	Co-40%Cu	3%

* predicted from the phase diagram

Fig. 1 : Phase Diagram for Cobalt Copper

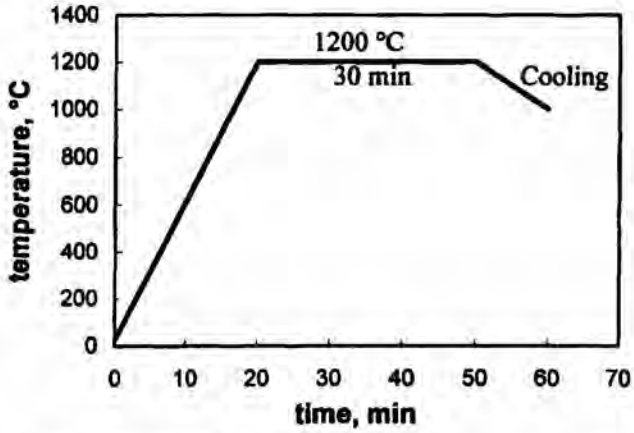

Fig. 2 : Temperature Pı file during microwave liquid phase sintering of Co-Cu alloy

3. RESULTS & DISCUSSION

Macrostructure

Figure 3 shows the macrostructure of all the Co-Cu samples after microwave sintering at 1200°C for 30 min. All the samples show a concave shape. It should be noted that the distortion in Co-20Cu shows higher distortion than Co-10Cu, while Co- 30Cu and Co-40Cu are slightly more distorted. This is in sharp contrast to the conventionally LPS alloys wherein Co-10Cu and Co-20Cu were able to maintain a cylindrical shape, the Co-30Cu alloy was only slightly distorted and Co-40Cu alloys was excessively distorted. The distortion profile for all the samples are shown in Figures 4a and 4b. To show the relative dimensional changes during sintering, the measured sectional diameter and heights were normalized with respect to the initial diameter (Do) and height (Ho) of the green cylindrical compact in Fig. 4a. In Fig. 4b, the final maximum diameter (Dmax) and maximum height (Hmax) of the sintered samples were used to normalize the measured sectional diameter and heights respectively. The distortion profiles also confirm the observations made above.

Any LPS can be described in terms of two important events: densification and distortion, and these events have been found to occur in a sequence [10,11]. Once the melt formation occurs, capillary forces act on the system cause rapid densification. These capillary forces also provide sufficient rigidity to the system to resist any distortion. However, once full densification has been achieved this capillary force becomes nonexistent [12]. At this stage, if the compact does not have sufficient rigidity, i.e. if sufficient solid-solid bond formation has not occurred, the system will not be able to resist viscous flow and will distort [13,14]. This was the cause for distortion observed in conventionally sintered Co-Cu alloys. However, in the present case, the presence of rounded microporosities in all the samples indicate that full density has not been achieved in any of the samples. Thus the distortion has not occurred subsequent to full densification. The cause for this distortion is not clear at this time.

Fig. 3 : Photographs of Co-Cu alloy after microwave sintering at 1200°C for 30 min. : (a) Co-10% Cu, (b) Co-20%Cu, (c) Co-30%Cu and (d) Co-40% Cu

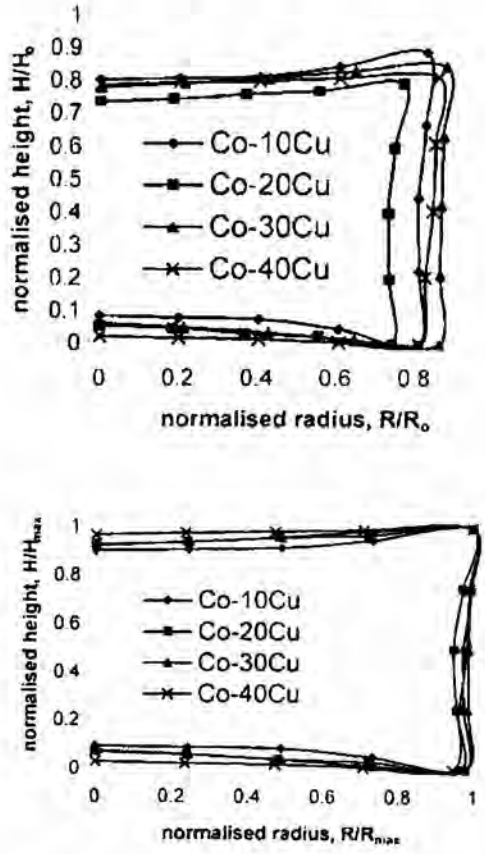

Fig. 4 : Distortion profile of Co-Cu alloy after sintering at 120°C for 60 min.

Densification Analysis

The results of the densification analysis have been tabulated in Table 1. Archimedes principle measurements were used to calculate the volume of sintered samples for accurate density determination. The results show that the densification achieved after 30 min of microwave sintering is much lower than after 60 min of conventional sintering. This is surprising as microwave sintering is generally expected to lead to faster densification. Conventional sintered Co-10Cu shows a densification parameter of 0.89 after sintering at 1200°C for 60 min. This indicates that the diffusion of Cu into Co does lead to swelling, as is the case in Cu-Sn system. Thus lower densification rate during microwave sintering cannot be attributed to the diffusion of Cu into Co at the sintering temperature. Moreover Roy et al. [5] were able to sinter pure Co powder to almost 100% theoretical density in 10 min using microwave sintering. It is therefore hypothesized that the formation of the Cu rich melt at the sintering temperature causes decoupling between the microwave and the Co-Cu compacts. Similar hypothesis was also resulted for premixed and prealloyed microwave sintered Cu-12Sn [8].

were seen in Co- 30%Cu and Co-40%Cu. Figure 6 shows the microstructure of the sintered samples. No evidence of density induced segregation is observed in any of the samples. However a copper 'sweating' phenomenon is observed in Co-30Cu and Co-40Cu. The liquid has segregated on the periphery of the samples. A much thicker layer has segregated on the periphery in Co-40Cu as compared to Co-30Cu. Figures 7 and 8 show the liquid segregation in Co-30Cu and Co-40Cu respectively. The rapid heating rate in case of microwave heating does not give sufficient time for the formation of solid-solid bonds. Once the melt formation occurs at the sintering temperature, the structure is highly porous, enabling the liquid to flow freely in all directions. Thus the liquid segregates at the periphery of the sample.

It should also be noted that the grain size in all the microwave-sintered samples is much smaller compared to the conventionally sintered samples. This was expected as microwave sintering leads to faster heating as well as cooling rate which gives less time for grain coarsening to occur. Moreover, microwave sintering (30 min) was done for a shorter time period compared to conventional sintering (60 min)

Sample	Greem Demsity		Sintered Demsity		Desification Parameter
	(gcm^3)	(% Theoretical)	(gcm^3)	(% Theoretical)	
Co-10Cu	4.76	53.4	6.75	75.8	0.48
Co-20Cu	4.87	54.6	7.38	82.9	0.62
Co-30Cu	5.06	56.7	6.73	75.6	0.44
Co-40Cu	5.20	58.3	6.5	72.9	0.35

Table 1 : Densification analysis

Microstructure

Figure 5 shows the sectioned view of sintered compacts. The figures indicate the presence of microporosity in all the alloys, while no macropores are seen. This is in contrast to the conventionally LPS alloys where large macropores

Stereological Characterization

All the results of the stereological characterization have been reported inTable 2. The connectivity and the contiguity decreases with increasing copper content. While the contiguity of the microwave sintered samples follows the

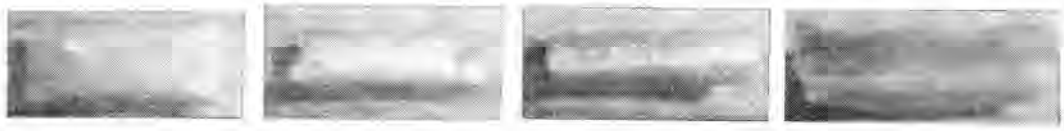

(a) (b) (c) (d)

Fig. 5 : Sectioned view of the microwave LPS sintered Co-Cu compacts : (a) Co-10%Cu, (b) Co-20%Cu.

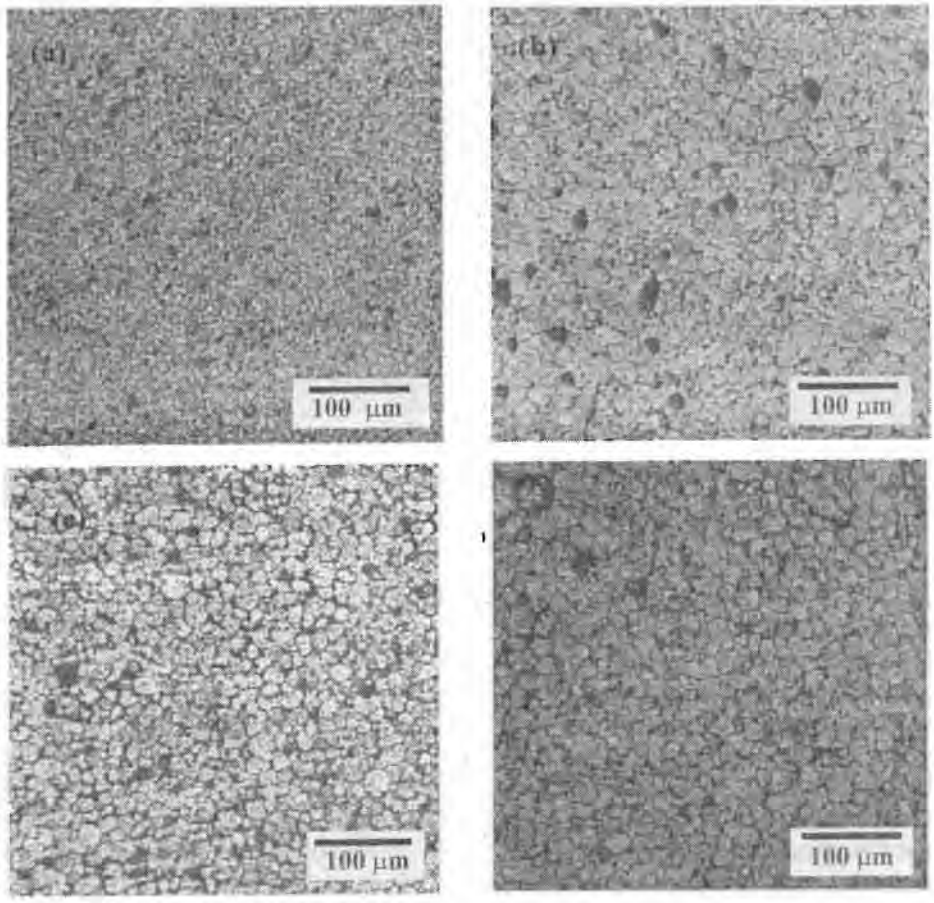

Fig. 6 : Optical micrographs of (a) Co-10Cu, (b) Co-20Cu, (c) Co-30Cu and (d) Co-40Cu after microwave sintering for at 1200°C for 30 min.

Sample	Coordination Number (C_c)	Dihedral angle ()	Contiguity (C_g)	Fraction Solid Content (V_s)
Co-10Cu	—	—	—	93.2%
Co-20Cu	3.15	38.1 ±13	0.40 ±0.13	85.2%
Co-30Cu	1.85	41 ±12	0.192 ±0.13	68.5%
Co-40Cu	1.43	34.7 ±13	0.159±0.14	66.2%

Table 2 : Sterological characteristics of the conventionally sintered samples

same trend as the conventionally sintered samples, the connectivity follows a different trend. The formation of large 'pools' of the liquid phase and subsequent localized segregation resulted in the higher contiguity in case of conventionally sintered Co- 40Cu compared to Co-30Cu. However, as no such events have occurred during microwave sintering, the connectivity decreases with increasing liquid (copper) content. The volume fraction of the solid phase in Co-30Cu and Co-40Cu is approximately the same. This is attributed to the segregation of the liquid at the peripheries, resulting in an apparent increase of the solid content in the remaining sample.

4. CONCLUSIONS

The result of the present study demonstrates surprisingly different trends in the microstructural and macrostructural evolution during conventional and microwave LPS of Co-Cu alloys. While conventional sintering occurs in a

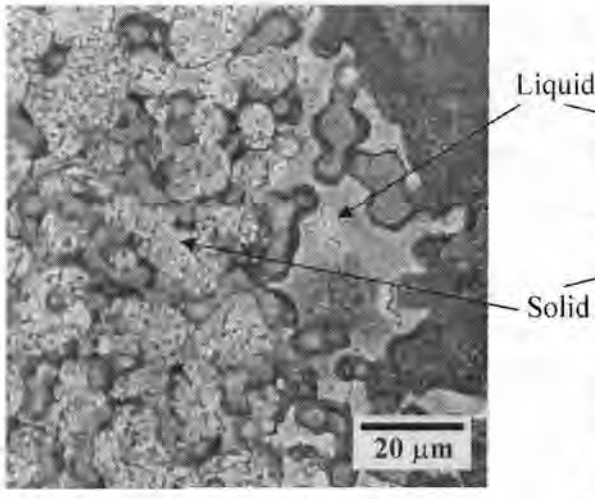

Fig. 7 : Liquid segregating at the peripheries of as microwave sintered Co-30Cu

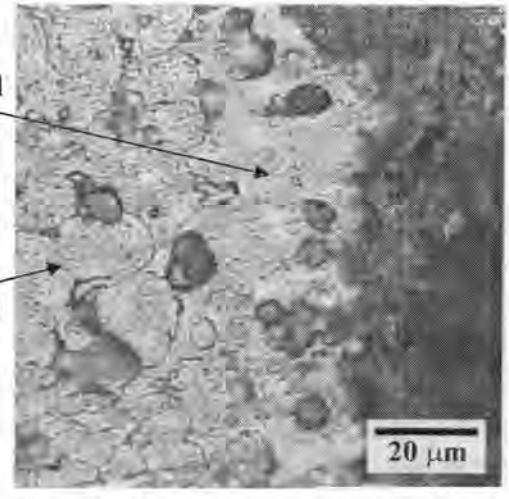

Fig. 8 : Liquid segregating at the peripheries of as microwave sintered Co-40Cu

sequence of events – namely, formation of melt leading to rapid densification, and then distortion/ macrosegregation – microwave LPS appears to undergo an entirely different sequence of events. In microwave LPS, densification and microstructural segregation and macrostructural distortion seem to occur at the same time. The mode of distortion is not clear at this time. The higher heating rate in microwave sintering favours the formation of a finer microstructure, but leads to low solid-solid bond formation, which in turn results in 'sweating' of the liquid phase on the periphery of the sample. Contrary to conventional believes, microwave sintering does not lead to faster or higher densification during LPS of Co-Cu alloys, indicating that this process is applicable to certain systems only. Finally, the results of this study and others seems to indicate that an alloy melt formation causes decoupling between the microwave and the material, arresting the sintering process.

REFERENCES

1) W.H. Sutton, "Microwave Processing of Ceramic Materials," Ceram. Bull.,v.68,n.2,1989, pp.376-384

2) K.J. Rao and P.D. Ramesh, " Use of microwaves for the synthesis and processing of materials," Bull. Mater. Sci., v.18, n.4,1995, pp. 447-465

3) D.E. Clark W.H. Sutton, " Microwave Processing of Materials," Ann. Rev. Mater. Sci., v.26,1996, pp. 299-331

4) R. Wroe, "Microwave Sintering coming of Age," Metal. Powder Rep. , v.54,n.7/8,1999,pp. 24-28

5) R. Roy, D.K. Agarwal, J.P. Cheng and S. Gedevanishvili. "Full sintering of powdered metals using Microwaves," Nature, v.399, n.17, 1999, pp.668-670

6) S. Gedevanishvili, D.K. Agarwal and R. Roy, " Microwave combustion synthesis and sintering of intermetallics and alloys," Mater. Sci. Lett.

7) R.M. Anklekar, D.K. Agarwal, and R. Roy, " Microwave sintering and properties of PM Copper Steel," Powder. Metall., 2001, v.44, n.4, pp.355-362

8) A. Upadhyaya, G. Sethi, H. Kim, D.K. Agarwal, and R. Roy

9) P. Garg, A. Upadhyaya, "

10) W. Yi, D.F. Heaney, R.G. Iacocca, R.M. German, "Linking microstructure and macrostructure during LPS under gravity." MPR 2000; 10-15

11) X. Xu, A. Upadhyaya, R.M. German, R.G. Iacocca, "The effect of porosity on distortion of liquid phase sinteted tungsten heavy alloys," Inter. J. Refractory Metals & Hard Mater. 1999; 17: 369-379

12) J. Liu, A.L. Cardamone, R.M. German, "Estimation of capillary pressure in liquid phase sintering," Powder Metall. 2001: 44:317-324

13) J. Liu, R.M. German, "Densification and shape distortion in Liquid Phase Sintering," Metall Mater Trans A 1999;30A:3211-3217

14) J. Liu, A. Upadhyaya, R.M. German, "Application of percolation theory in liquid phase sintering: II. Prediction of shape distortion under ground base sintering," Metall Mater Trans 1999;30:2209-2220

Cu-Co-Fe PRE-ALLOYED POWDER AS A MATRIX MATERIAL FOR DIAMOND TOOOLS

R. R. Thorat*, P. K. Brahmankar* and T. R. R. Mohan,**

*Dept. of Mechanical Engg, Dr. Babasaheb Ambedkar Technological University, Lonere, Raigad-402 103,
**Dept. of Metallurgical Engg. & Materials Science, Indian Institute of Technology, Bombay, Powai, Mumbai-400 076

ABSTRACT

In the present investigation, the consolidation behavior of Cu-Co-Fe pre-alloyed powder for the diamond tools is discussed. Diamond-pre-alloyed powder composites were prepared by cold pressing followed by pressureless sintering and hot isostatic pressing (HIP). The synthesized powder contained two phases; copper as a major phase and cobalt-iron as a minor phase. The compaction behavior of the powder was slightly affected by the addition of 2 wt % of diamond to the powder. The smaller particle size and higher weight percentage of copper in the powder resulted into the better densification and consequently higher sintered density.

Keywords: Cu-Co-Fe Prealloyed Powder, Diamond Tools, Pressureless Sintering and Hot Isostatic Pressing

1. INTRODUCTION

The productive usage of diamonds within the cutting tool depends on the capability of the matrix to hold the diamonds and thus its support to cutting process. There is no universal, all-purpose bond. In practice, every tool manufacturer employs his own thoroughly tested compositions and sintering compositions. Metal bond constituents in widespread use are based on copper and copper alloys, iron, cobalt, as well as high-melting point carbides and metal powders. The presence of carbides and high melting point metals fillers (e.g. Ti, Cr, W, Zr, Si and Mo) in tool matrix increases the abrasion resistance. Besides, powder characteristics such as particles size distribution, particle shape and sinterabilty also affects the selection of the binder for stone and rock cutting application [1, 2].

The cobalt metal powder, used in industry as a matrix material for granite cutting diamond tools, is an expensive and strategic material. Therefore, since last ten years, the research is focused on developing the alloy powders, which could be the alternative or at least reduce the content of the cobalt in diamond tools. The development of pre-alloyed powders as a diamond tool matrix is the result of this ongoing research [3]. Commercially available powders containing Cu, Co and Fe in predetermined ratios have been produced and used in the construction diamond tools e.g. floor sawing, wall sawing and core drilling of reinforced concrete and asphalt. These powders can be processed exactly in the same equipment as usual cobalt powders. Due to sub-micronic size of these powders, the maximum density and hardness are achieved at temperatures as low as 650°C, which offer several possibilities of savings [4,5].

2. EXPERIMENTAL PROCEDURE

Following the conventional route, the experimentally developed Cu-Co-Fe pre-alloyed powders were first dry mixed with 0.7wt % of an organic binder (PVA) as a pressing aid. Mixing was carried out using mortar and pesters. Diamond particles of 40-60 US mesh were subsequently mixed in a concentration of 2wt %. The compaction behavior of the synthesized powder mixture was studied by die pressing cylindrical green specimens at 500MPa pressure. Pressureless sintering of the specimens was carried out at 950°C for two different heating rates (5°C /min and 10°C /min). It was followed by hot isostatic pressing (HIPing) at 100MPa and 900°C in argon atmosphere for 30 minutes. The X-ray diffraction analysis of the powder samples was carried by PHILIPS PW 1800 XRD unit, using copper target (wavelength = 1.54 A°). The chemical composition and microstructure of the pre-alloyed powder was analyzed by using FEI and Jeol JSM 840A scanning electron microscope (SEM) attached with energy dispersive spectroscope (EDAX). The particle size of the powders was determined by laser particle size analyzer, GALAI-CIS-1.

3. RESULTS AND DISCUSSION

3.1 Characterization of the Cu-Co-Fe prealloyed matrix powder

Figure 1(a) shows chemical analysis of the Cu-Co-Fe powder with anticipated proportions of the copper, cobalt

and iron. Carbon and oxygen are also present as impurities. The theoretical density of the Cu-Co-Fe pre-alloy (8.33 g/cc) is lower than that of cobalt alone (8.9 g/cc). This shows that the use of Cu-Co-Fe pre-alloyed powder could allow savings on raw material cost. X-ray diffraction pattern of the synthesized pre-alloyed powder (figure 1(b)) shows two phases; copper as a major phase and cobalt-iron in the form of solid solution of cobalt in iron as a minor phase. The crystallite size of both phases is found to be equal (~25 nm) as determined by Debye-Scherrer formula. Copper is a continuous phase in the powder because of its limited solubility in the Fe-Co solid solution with bcc lattice for the given reduction temperature (650°C). The average particle size of the Cu-Co-Fe pre-alloyed powder is 3.3μm, which is less than that of commercially available pre-alloyed powder. Figure 1(c) shows SEM micrograph of Cu-Co-Fe powder. Powder particles are in the form of irregular shaped agglomerates, which is a characteristic of the powder prepared by pyroletic technique. The agglomeration of the powder particles is due to the high surface area and the action of chemical and mechanical forces.

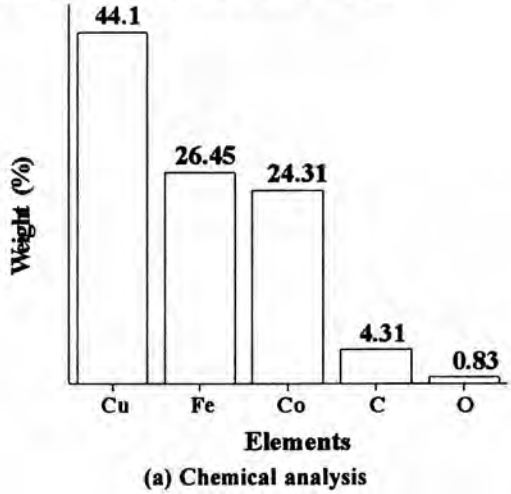

(a) Chemical analysis

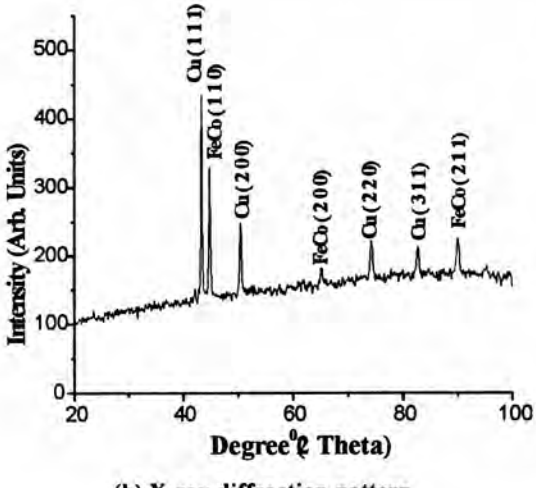

(b) X-ray diffraction pattern

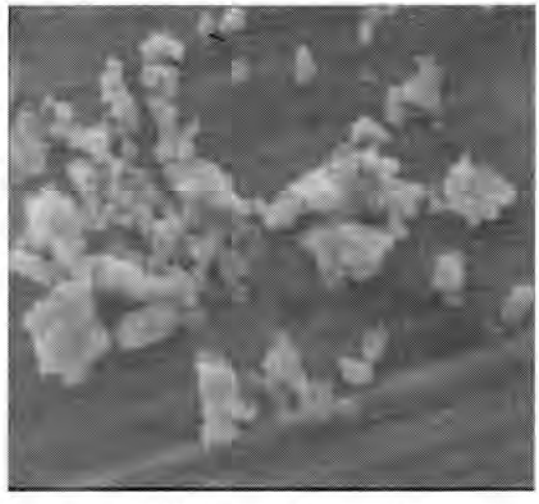

(c) SEM images of the powder

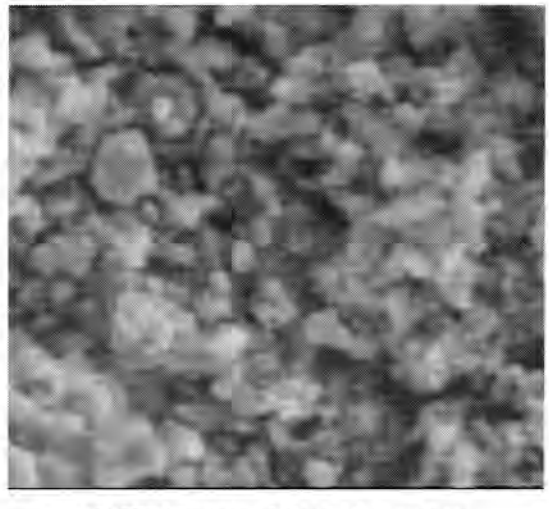

(d) SEM images of sintered compacts

Fig. 1 Characterization of synthesized Cu-Co-Fe pre-alloyed powder

3.2 Compaction studies

Figure 2 shows the variation of the green density of the powder compacts without addition of diamond against the applied pressure. The plastic flow of copper helps to increase the contact area between irregular particles and the creation of interparticle locking. Also, the presence of hard Fe-Co phase leads to significant plastic deformation of copper and consequently a high green density. It is also noteworthy that the compaction behavior of the powder is slightly affected by the addition of 2wt % of diamond to the powder. At lower compaction pressure, the diamond

particles, which are extremely hard, oppose the compressive forces of compaction and consequently result into the decrease in green density of the pre-alloyed powder. However, at higher compaction pressure, diamond particles help to deform copper due to their large size and result into slight increase in green density as shown in fig.2.

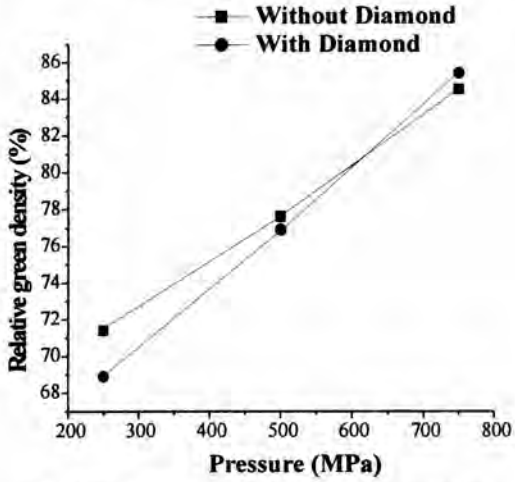

Fig. 2 Green density of Cu-Co-Fe powder as a function of compacting pressure

3.3 Sintering Studies

Figure 3 shows density variation of Cu-Co-Fe powder mixed with diamond powder sintered freely at different heating rates. The smaller particles size and higher weight percentage of copper in the Cu-Co-Fe powder leads to the better densification and consequently higher sintered density. It is the diffusion rather than plastic flow of copper, which is more dominant during sintering at high temperature (950°C). The sintering density of the powder is not significantly affected by the increase in the heating rate (from 5°C/min to 10°C/min). SEM images (Fig.1 (d)) of sintered specimens heated at 5°C/min shows non-geometrical sintering. The hot isostatic pressing (HIPing) without traditional glass encapsulation of Cu-Co-Fe - Diamond sintered specimens results maximum sintered density due to initial less amount of porosity (2.6 %). Full density is obtained for the specimens who were earlier sintered at 950°C in hydrogen atmosphere (heating rate: 10°C /min) and subjected to HIPing at 100MPa and 900°C in argon atmosphere for 30 minutes. The high sinterability of Cu-Co-Fe powders suggests the possibility of using pre-sintering followed by HIPing as an alternative fabrication route for pre-alloyed based diamond tools. Figure 4 shows the sites, from where the diamonds are dislodged due to impact loading. It is due to the plastic deformation (more ductility) of copper, which results into a weak holding of the diamond in the matrix. Figure also shows slight attack on the diamond surface due to pre-alloyed powder. The diamond / matrix interface indicates that the bonding between the diamond and powder is held by weak mechanical forces with little contribution coming from chemical bonding. However, it is important to note that no optimizations were made with varying diamond concentration and size or with respect to mixing other powders with Cu-Co-Fe powder, which could potentially strengthen the bonding.

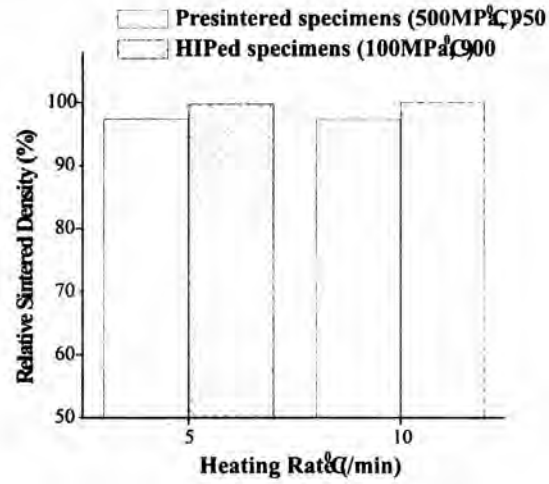

Fig. 3 Effect of hot isostatic pressing (HIPing) on Cu-Co-Fe - Diamond specimens presintered at different heating rates

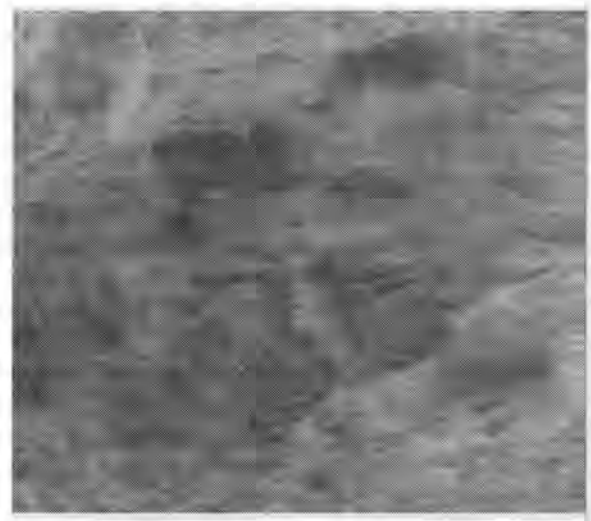

Fig. 4 Fractograph of the Cu-Co-Fe – Diamond Composite

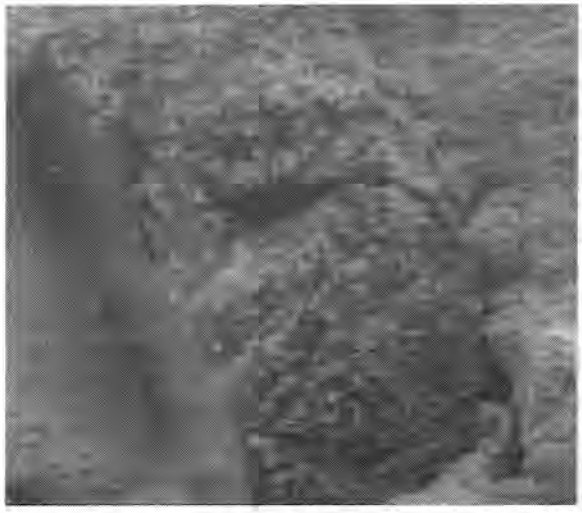

Fig. 5 Diamond particle in the Cu-Co-Fe matrix

4. CONCLUSIONS

1. The compaction behavior of the powder is affected by the plastic deformation of copper and the stress concentration effect produced by the presence of hard Fe-Co phase. At lower compaction pressure, the addition of diamond particles results into the decrease in green density of the pre-alloyed powder. However, at higher compaction pressure, diamond particles help to deform copper and result into slight increase in green density.

2. The smaller particle size and higher weight percentage of copper in the Cu-Co-Fe powder leads to the better densification and consequently higher sintered density.

3. Pressureless sintering followed by hot isostatic pressing maximizes sintered density of the Cu-Co-Fe - Diamond composite. It also suggests the possible route for processing of these pre-alloyed powders for the consolidation of diamond tools.

REFERENCES

1. A. Bakon and A. Szymanski, Practical Uses of Diamond, Ellis Harwood, pp.1-53, (1993).

2. P.A.Vityaz and L. V. Sudnik, "Diamond composites with low temperature binder for abrasive and blade tools", Proceedings of European Conference on Hard Materials and Diamond Tooling: Euro PM2002, Lausanne, Switzerland, Oct.7-9, (EPMA, UK, 2002), pp.63-67.

3. M. del Villar, P. Muro, J. M. Sanchez, I. Iturriza, and F. Castro, "Consolidation of diamond tools using Cu-Co-Fe based alloys as metallic binders", Powder Metallurgy, Vol.44, pp.82-90 (2001).

4. I. E. Clark and B. J. Kamphuis, "Recent Developments in Pre-alloyed Powders for Diamond Tooling", *ibid 2,* pp.35-42.

5. H. K. Tonshoff, H. Hillmann-Apmann and J. Asche, "Diamond Tools in Stone and Civil Engineering Industry: Cutting Principles, Wear and Applications", Diamond and Related Materials, Vol.11, pp.736–741(2002).

INJECTION MOULDING OF STAINLESS STEEL POWDERS

Aebgin John Poickattil and T.R.Rama Mohan

Dept. of Metallurgical Engg. & Materials Science, Indian Institute of Technology, Bombay, Powai, Mumbai-400 076

ABSTRACT

Metal Powder Injection Moulding (PIM) is increasingly becoming popular to process small and intricate shaped components. The success of the process depends on the availability of fine powders, lubricant and binder. The fundamental studies concerning this process are scarce in literature. The present paper reports some optimization studies in project of injection molding of stainless steel powders. The samples obtained were verified for consistency in weight. Studies were carried out in debinding the samples in solvents followed by thermal debinding. In the present investigation, different binder formulations and optimization of injection moulding parameters are discussed.

Keywords: Injection molding, Binder formulation, Debinding, Sintering

1. INTRODUCTION

Powder injection moulding (PIM) uses the shaping advantage of injection moulding but is applicable to metals and ceramics. Metal Powder injection moulding (MPIM) process is drawing much attention as a promising technique which leads to a large-scale production of metalworking with precision and complex in shape[1]. MPIM is a technology currently used in several industrial applications that brings together the diversity of conventional powder metallurgy (P/M) and geometric freedom of component design associated with thermoplastic injection moulding. The combination of these technologies allows complex shape for high performance applications. It is an elegant blend of plastic injection moulding, based on the use of fine powder particles mixed with waxes and/or thermoplastic polymers to form a feedstock that can be moulded. The granulated feedstock is then given a shape using an injection moulding machine. After shaping, the polymer binder must be removed from the moulded part without significantly disturbing the powder particles. Then the powder is sintered at high temperatures, often to near theoretical densities. This technology provides an alternative method for producing small, complex, precision parts, cost effectively in high run volumes. Advantages of MPIM include: greater design flexibility, closer tolerances and more uniform shrinkage after sintering[1]. This industry has established a commercial credibility in the production of many components and it is clear that major growth occur for several types of products ranging from automotive to consumer products.

PIM is still in a developing stage. It would be most appropriate to call PIM as an ever-evolving manufacturing process, because of the developments in the design of injection moulding machines, injection moulding pressures, binder formulations, debinding methods, etc. A new area of exploration for the process is the production of micro sized parts, which should help meet future medical needs as parts continue to shrink for minimally invasive surgery. The process is generally best suited to parts measuring less than 6 mm thick and weighing less than 100grams. Newer techniques, however, have enabled the processing of cross sections above 12.5 mm and up to 400 grams.

Stainless steel is one of the most widely used materials for MIM research and industrial applications. Since 316L stainless steel is a highly alloyed material, the mechanical and corrosion properties are a concern. Therefore, a high final density is important for optimization of the desirable attributes[2]. In the present work Stainless steel components are prepared by injection moulding process and optimize the injection moulding, post injection moulding and sintering conditions for achieving high quality and cost effectiveness in the process. Novel binder formulation, debinding studies through ,vacuum,solvent and thermal methods have been carried out. So far thermal debinding has emerged as a promising option. The chemical composition and microstructure of the powder was analyzed by using FEI and Jeol JSM 840A scanning electron microscope (SEM) attached with energy dispersive spectroscope (EDAX). The particle size of the powders was determined by laser particle size analyzer, GALAI-CIS-1.

2. EXPERIMENTAL WORK

Stainless steel (316L) powders of different particle size an different surface morphologies are characterized and mixed together to get maximum tap density.The two types of powders used were water atomized which have mean particle size of 8.55 microns and 6.73 microns respectively. The maximum sizes were of 17.00 microns and 12.80 microns respectively.

The binder plays an important role, next only to the powder characteristics, in the injection moulding process. The basis for the selection of the constituents of the binders was to facilitate further processing, particularly the debinding. Multi component binders are preferred over single component binders as different thermal properties of the several constituents help in progressive removal of the binder and prevent the shape loss of compact during debinding. Table 2 .1 lists the binders and its base.

Binder	*Base*
Bin#1	Wax
Bin#2	Polyethylene Glycol

Table.2.1 Binders and their base.

Bind#1and 2 was made by melting of the wax granules in a beaker by heating upto75°C . PEG and stearic acid were added into the melt and stirred till a uniform melt was obtained.The melt was pressed to form small pellets

The powders and binder is mixed to make a uniform and homogenous feedstock of the. Ideally every powder particle should be wetted by the binder. Z,S type sigma blade mixer is used to mix feedstocks for powder injection moulding. These mixers have the capability of hot mixing. The mixer has a volume of 500 ml with heating upto 200 °C. It is capable of giving a variable rotational speed. Bind#1and 2, being in pellet form, was mixed with the stainless steel powder and then heated in an oven at a temperature of 95°C. This was intermittently stirred with a steel spatula to prevent agglomeration.The feedstock prepared was in the pellet form.

Initial attempts to injection mould feedstock of stainless steel powder with 8wt % Bind# 1 did not give good results. Subsequently the binder content was increased to 10%. Varying injection parameters like injection pressure and temperature ,finally defect free samples were obtained. Subsequently, Bind# 2was considered for preparing the feedstock The method has already been explained earlier. Feedstocks prepared along with their binder composition are given in Table 2.2.

Sr no	*Feedstocks prepared*
1.	SS+ 9 wt % Binder 1
2.	SS+ 9 wt% Binder 2
3.	SS+ 10 wt% Binder 1
4.	SS + 10 wt% Binder 2

Table 2.2 Feedstocks and binder content

Thereafter feedstocks were successfully injection moulded and their densities calculated.

Debinding of the SS+ 10 wt% Binders 1&2 compacts was studied by various methods viz. vacuum, wicking and thermal debinding. SS+10 %Binder 2 were studied by water leaching and thermal debinding.

Vacuum +Thermal Debinding was carried out in a vacuum oven, which was operated with a rotary pump. The compacts were kept in vacuum of the order of 600 Kg/cm^2 vacuum pressure and heated upto 230°C at a rate of 10°C / hour. The change in weights of the compacts was noted and % binder loss calculated.

In Solvent debinding ,the solvents used for the study were those with solubility for atleast one of the constituents of the binder.

Distilled water leaching.

Compact with binder 1and 2 was leached in distilled water to remove PEG. The compact were immersed in distilled water for different durations-5, 10 and 15 hours and the weight loss was measured. Then the compact were immersed in warm water (45°C) for 5 hours. The PEG wt loss observed to be very fast.

In **Thermal debinding**, first trial was done in air at a rate of 10°C/hour. The temperature was kept at 450°C for a time of 1 hour. but it caused melting of the sample ,so the rate was reduced to 5°C/hour, eventhough there was no melting ,there was some shape deformation, so vacuum debinding in lower temperatures were tried and was successful. Direct thermal debinding was tried with extremely low rates like 1-2 °C/hour, there was no sample melting but it took more time for debinding.

The compacts that were thermally debound were chosen for sintering. Sintering was done at 1320°C with a holding time of 1 hour in Ar atmosphere. Results and discussion of these experiments are given in the following chapter.

RESULTS AND DISCUSSION

3.1 Characterisation of Stainless steel powder

The powder used was water atomized SS316L ,supplied by Indo –US : MIM ,Bangalore. Powders of different particle sizes and shapes are mixed together to get maximum tap density. The average particle of ***SS316L-1*** powders was 8.55 microns and its specific area was 6.6x 10^{-1} cm^2/ml. The had an average size of 6.73 microns and surface area

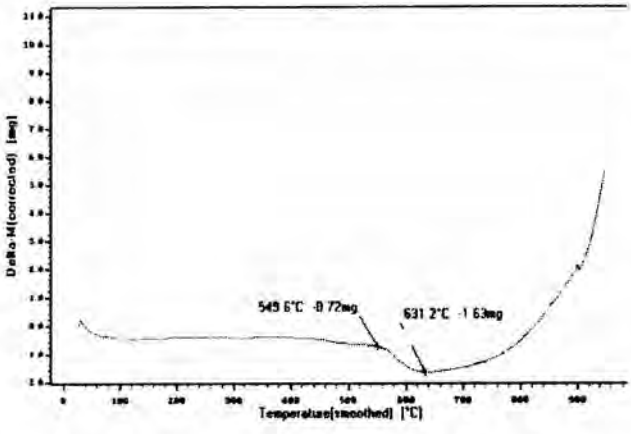

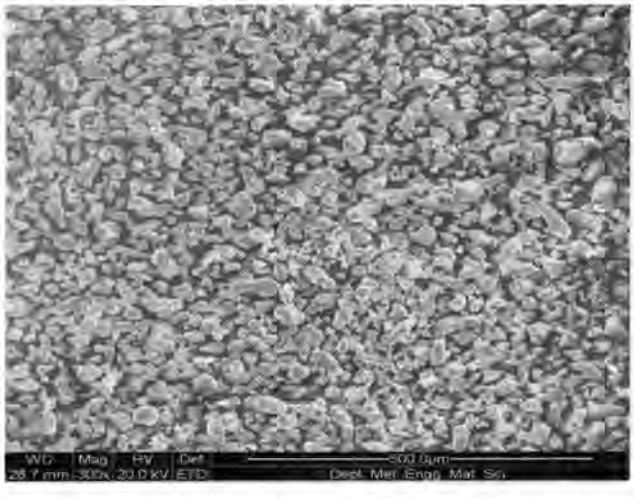

Figure 3.1 TGA of SS upto 1000° C and ESEM micrograph of SS powder

of 8.3x10^{-1} cm^2/ml for ***SS316L***-2 powders. The combination of particles of two different sizes would give denser compacts as compared to particles of same size.

The TGA result of SS heated in air upto 1000°C at the rate of 10°C/min, shown in Fig 3.1. It is important to note that at a temperature of 630°C, the oxidation is started This analysis was done to check the possibility of thermal debinding in air.

An ESEM of SS powder is shown in Fig 3.1. A combination of equiaxed and elongated particles is seen. This would aid in increasing the debinding rate. Surface energy of such particles is lower than that of spherical particles. Spherical particles are associated with slow debinding since they have highest surface energy.

3.2 Characterisation of Binders

The constituents of the binders were checked for solubility in various solvents. Table 3.1 lists the constituents and their solvents.

Table 3.1 Binder constituents and solvents

Constituents	*Solvent*
PMMA	Acetone
PEG	Water
Stearic Acid	Acetone
Wax	CCl_4,Xylene,Toluene

The purpose of these studies was to adopt solvent debinding as standard method of debinding. Binders prepared were also checked by TGA to understand their thermal degradation characteristics. This was important to assess the feasibility of thermal debinding.

Fig 3.2 shows the TGA curve for Binder 1. It shows a binder loss of nearly 50% at 270°C and it undergoes almost complete decomposition by 499° C.

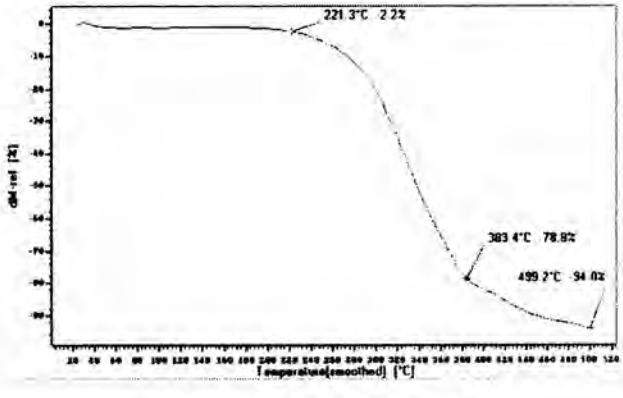

Figure 3.2 TGA of Binder 1

3.3 Injection moulding of Stainless steel powders

The injection moulding process parameters optimized for the study is given in Table 3.2.For different binder systems ,the optimized injection moulding parameters are different.

Parameters	*bin#1*	*bin#2*
Injection temperature	240° F	360° F
Injection pressure	500 KPa	650 KPa
Clamp pressure	270 KPa	270 KPa
Injection time	2 sec	3 sec
Clamp time	4 sec	5 sec

Table 3.2 Injection moulding parameters for SS powders

3.4 Debinding and Sintering

Vacuum + Thermal debinding

Samples with the Binder1 showed a progressive binder loss upto 10 hours of holding in vacuum at 0.7Kg/cm2 and temperature of 65°C. Starting with 1.2 % loss within 1 hour maximum loss obtained was 11.4 % after 14 hours as shown in Fig 3.3.

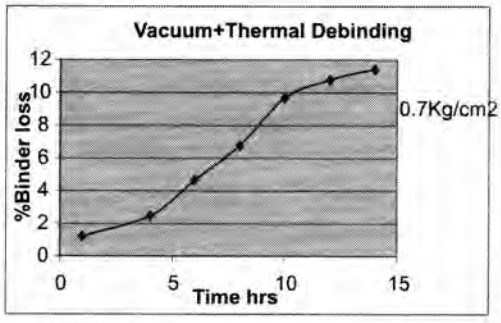

Figure 3.3 Effect of debinding in vacuum at 65 °C

Solvent debinding

The major constituent of the Binder 2 exhibited good solubility in water.The debindig was accelerated by heating water to 60 °C

Water had a very slow rate of debinding with excellent shape retention.. As much as 12.9% binder loss was observed, this is shown in Fig 3.4.

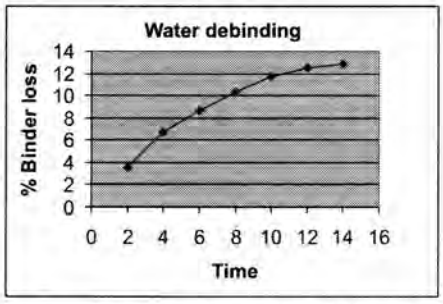

Figure 3.4 Effect of Water debinding

Thermal debinding

Thermal debinding of compact followed by sintering, both in air and in argon atmosphere did lead to complete binder loss. There was no interparticle bonding in the case of direct debinding and sintering in air. The sintered mass was in the form of loose powders. Oxidation of the stainless steel particles must have taken place.

Thermal debinding in Ar atmosphere with a holding time of 1 hour at 100°C partially melted the sample., but slow rate of heating and cooling helped in retaining the shape of the compact. As a slow rate of heating is maintained the interface between the binder and powder gradually recedes, giving a network of porosity towards the end of debinding. As sintering proceeds, the porosity shrinks and interparticle bonding occurs. The binder loss at the end of thermal debinding was considerable. Fig 3.7 shows the binder removed from the compact..The ESEM photograph of injection molded and debinded compact is shown in fig 3.5

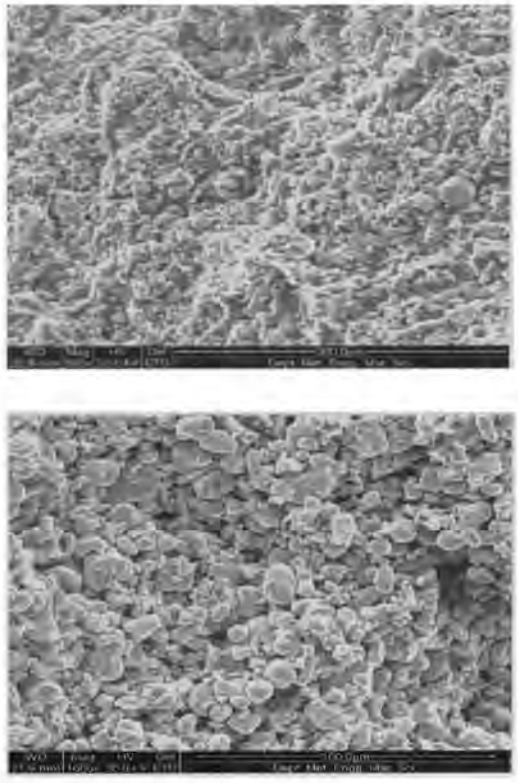

Figure 3.5. ESEM photograph of injection molded and debinded compact

The experiment was repeated with the compact covered in investment powder at extremely slow rate of 1°C/min upto a temperature of 400°C.It was held for 1 hour for debinding and then sintered at 1320°C for 1 hour. The cooling rate for this cycle was extremely slow i.e furnace cooling. A visibly defect free sintered compact was obtained. The sintering time of 1 hour was found to be insufficient for densification.

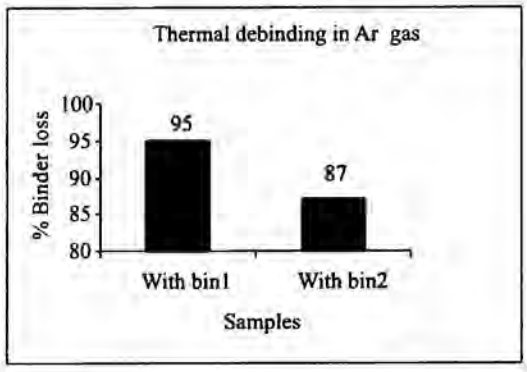

Figure 3.6 Effect of thermal debinding

CONCLUSIONS

- PEG based binder with a composition of 60%PEG + 20%Poly Wax +15% ParafinWax + 5% Stearic acid gives good results in solvent debinding.
- Powder-loading of 91% results in high green density, but beyond this the feedstock will become too cohesive for successful injection moulding.
- Powder size of maximum 15 microns and a distribution of 6 to 13 microns will results in successful injection moulding.
- Compacts with fine particle size exhibit a slow rate of debinding.
- Solvent debinding tried in the study can be used for partial debinding, and for complete binder removal thermal debinding should be done.
- Use of distilled water as solvent for debinding decreased the total debinding time and it is preventing deformation of compact during thermal debinding
- It is very important to maintain an extremely slow rate of heating during thermal debinding. This is more crucial when low melting constituents are present in the binder.
- Debinding and sintering in hydrogen atmosphere is comparatively suitable for stainless steel.

REFERENCES

1. M.A. Omar,R. Ibrahim, M.I. Sidik, M. Mustapha, M. Mohamad, Stainless steel injection moulded components, Journal of Materials Processing Technology 98 (2000) 325–335,2000
2. Yimin Li , Shaojun Liu, Xuanhui Qu, Baiyun Huang, Processing of 316L stainless steel powder injection moulding compacts, Journal of Materials Processing Technology 137 (2003) 65–69, 2001

SYNTHESIS OF PMN-PT CERAMICS FROM $MgNb_2O_6$ PRECURSOR

SUJAL UPADHYAY*, T. R. RAMA MOHAN**

*University of Mumbai, Mumbai

**Dept. of Metallurgical Eng. and Materials Science, IIT Bombay, Mumbai.

ABSTRACT

Lead based electroceramics are difficult to prepare reproducibly due to lead oxide losses during sintering. Lead Magnesium Niobate-Lead Titanate (PMN-PT) with pure pervoskite phase is difficult to prepare. Evidence for the formation of an intermediate Mg-containing pyrochlore phase, which coexists with PMN pervoskite along with unreacted PbO, is found when the reaction is carried out at lower temperatures. Attempts are made to prepare pyrochlore free PMN by solid state reaction of individual oxides. The phase analysis results are discussed. Lead Titanate (PT) is used as a phase stabilizer.

INTRODUCTION

The relaxor ferroelectric Lead Magnesium Niobate (PMN) was first investigated in the late 1950 [1]. The current motivation for the development of PMN is due excellent dielectric properties (ϵ = 12,000 at -15° C), broad maxima at curie point and low firing temperature (1100° C) [2-3]. Due to these properties they are emerging as potential candidates for multilayer ceramic capacitors and other applications. However these compounds are difficult to synthesize reproducibly pure pervoskite PMN. Undesired pyrochlore phase, which lowers its dielectric properties, is always found to be accompanied with pervoskite phase due to: (1) low chemical reactivity of MgO, (2) evaporation of PbO above 800° C and (3) unreacted Nb_2O_5 reacts to form pyrochlore phase [4-5]. Conventional solid state reaction leads to the formation of PMN with 20% pyrochlore phase. Synthesis of PMN by coloumbite method reduced the pyrochlore phase to 1-3%, developed by Swartz et al. [6]. Addition of excess MgO can further suppress the pyrochlore phase, but unreacted excess MgO segregates in the grain as well as in the grain boundary [7], which could significantly affect the dielectric properties. Among all the methods reported so far for the synthesis of PMN, columbite method [8] has proved to be the most successful method, since it gives nearly single (pervoskite) phase PMN. However inhomogeneous mixing in the coloumbite method leads to the formation of secondary phases and decreases dielectric properties.

Lead titanate (PT) with tetrahedral structure is used as a phase stabilizer and also to increase the dielectric properties. It is prepared by solid state reaction between oxides. xPMN-(1-x)PT systems are used in the capacitors. The systems with PT more then 0.3 are piezoelectric, whereas the ones around 0.1 PT have high dielectric properties.

EXPERIMENTAL

Synthesis of PMN was carried out by columbite method. The reactants used were MgO, PbO, TiO_2 (all Merck grade), Nb_2O_5 (buryone high purity 99.9%).

Initially, the precursor Magnesium Niobate (MN) with chemical formula $MgNb_2O_6$ was prepared. PbO & Lead Titanate (PT) were added to it to form xPMN-(1-x)PT system.

The synthesis is divided into 3 parts: 1) synthesis of MN, 2) synthesis of PT, 3) synthesis of PMN-PT.

All the reactants were mixed in mortar pestle. Acetone was used as a mixing media. The mixing time was 45min-60min. The mixture was then compacted in a cold hydraulic press at 60KN/m^2 using 13.6mm cylindrical dye. Steric acid was used as a lubricant. Each time the dye was cleaned with acetone and lubricated using steric acid. All samples were characterized by XRD using PHILIPS PANalytical instrument using Cu $K_v$wavelength or radiation (1.54056Å).

1) The reactants MgO and Nb_2O_5 were mixed in stoichiometric proportion, compacted and calcined at 900° C for 2 hours in stagnant atmosphere and sintered in the form of pellets at 1100° C and 1200° C in stagnant air and oxygen atmosphere up to 18 and 21 hours respectively, with intermediate grinding at regular intervals of 3 hours. Each time the pellets were crushed, mixed and compacted in the form cylindrical pellets. The temperature and sintering time

was optimized. 2) PT was formed by mixing the reactants PbO and TiO_2 and sintering at different temperatures (600° C & 700° C 2 hours). 3) MN formed was then mixed with PbO with 6 & 8 mole % excess and TiO_2 in stoichiometric proportion, compacted and sintered at 800° C for 3 hours to it to produce 0.9PMN-0.1PT system. Phase analysis of all samples was done from XRD data. A flowchart for the synthesis of PMN-PT system is shown in fig.1.

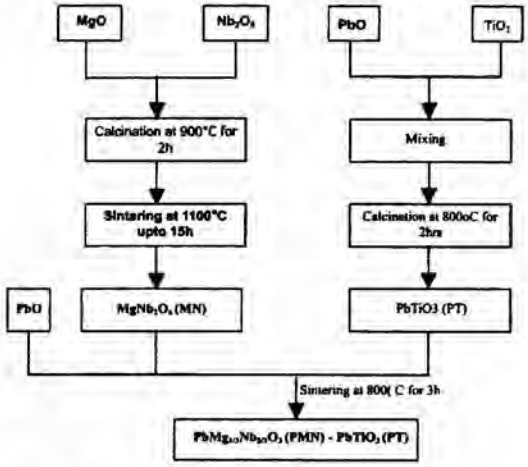

Fig. 1: Flowchart of synthesis of PMN-PT.

RESULTS AND DISCUSSIONS

The XRD after calcination shows that apart from the desired $MgNb_2O_6$ phase, many undesired phases like oxygen deficient $Mg_2Nb_6O_{11}$, unreacted Nb_2O_5 and MgO were found, indicating that the reaction is not complete. The amount of Nb_2O_5 was more as compared to MgO indicating the formation of secondary and non-stoichiometric phases. The XRD pattern of MN calcined at 900° C for 2 hours is as shown in fig. 2. From the figure it can be seen that the amount of Nb_2O_5 left is very high.

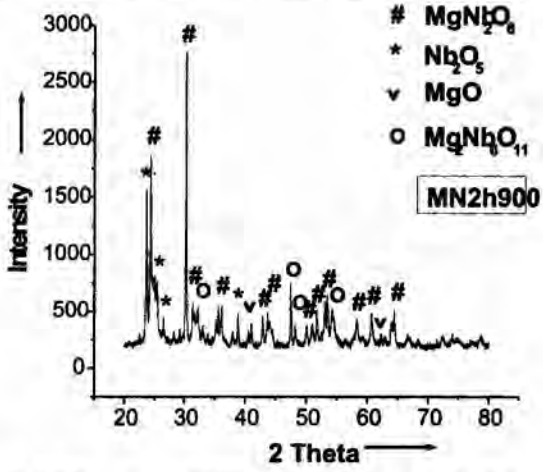

Fig. 2: XRD pattern of MN calcined at 900° C for 2 hours.

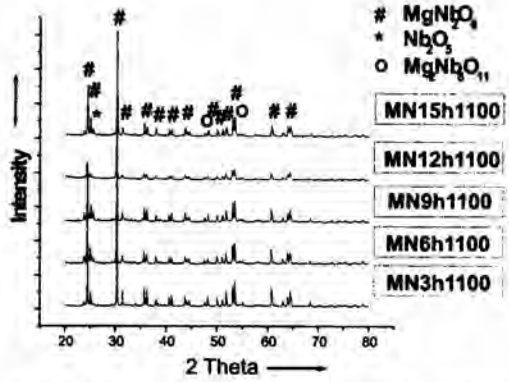

Fig. 2: XRD pattern of MN sintered at 1100° C up to 15 hours.

The calcined MN was sintered at 1100° C and 1200° C up to 18 and 21 hours respectively at a regular interval of 3 hours in stagnant atmosphere. The XRD data was obtained for all the samples are as shown in fig. 3 and 4.

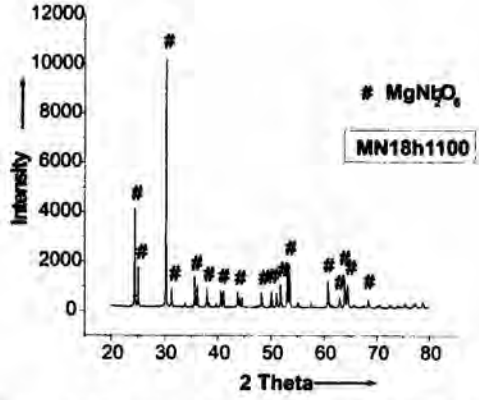

Fig. 3: XRD pattern of MN sintered at 1100° C for 18 hours.

The XRD (fig. 2) indicates that as the temperature increases, the amount of unreacted Nb_2O_5 decreases up to a minimum at 12 hours and then it again begins to increase for MN sintered for 15 hours. Unreacted MgO is not found as found after calcination. In the case of MN sintered at 1100° C for 18 hours (fig. 3), 100% compound formation has taken place, indicating the completion of reaction. However this could not be repetitively formed, which may be due to the inhomogeneous mixing of reactants.

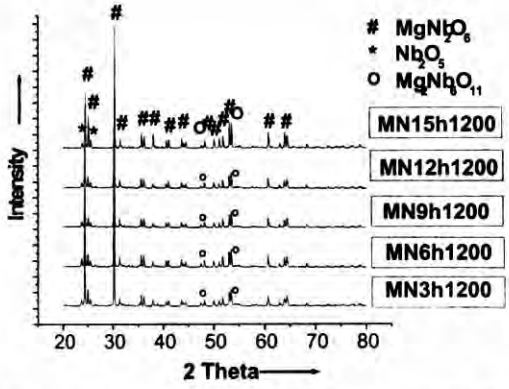

Fig. 4: XRD pattern of MN sintered at 1200° C up to 15 hours.

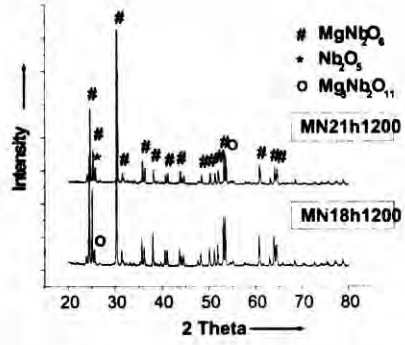

Fig. 5: XRD pattern of MN sintered at 1200° C for 18 & 21 hours.

In case of MN sintered at 1200° C the lowest amount of $Mg_2Nb_6O_{11}$ is found in MN sintered for 18 hours. Nb_2O_5 and MgO were not found. While the amount of MN formed decreases in the MN sintered for 21 hours. This may be due to the loss of oxygen or due to evaporation of MgO. So MN sintered for 18 hours is optimized for further synthesis. Different phases obtained in the synthesis of MN in percentage are shown in table 1 including calcination step.

Due to the formation of undesired oxygen deficient phase, it was decided to sinter MN in oxygen atmosphere. MN was sintered at 1200° C up to 18 hours in flowing oxygen atmosphere. Fig. 6 shows the comparison of XRDs of MN sintered in flowing oxygen atmosphere.

TABLE : Different phases obtained in the synthesis of MN in percentage.

Name	% of phases			
	$MgNb_2O_6$	Nb_2O_5	MgO	$Mg_2Nb_6O_{11}$
mn2h900	53.82	28.8	5.54	11.83
mn3h1100	83.38	9.70	4.06	2.87
mn6h1100	90.18	6.01	0.00	3.81
mn9h1100	88.95	7.80	0.00	3.25
mn12h1100	91.97	4.65	0.00	3.38
mn15h1100	91.80	5.48	0.00	2.72
mn18h1100	**100.00**	**0.00**	**0.00**	**0.00**
mn3h1200	88.87	7.30	0.00	3.84
mn6h1200	89.76	6.87	0.00	3.37
mn9h1200	91.03	6.10	0.00	2.87
mn12h1200	91.56	5.90	0.00	2.55
mn15h1200	94.22	3.31	0.00	2.48
mn18h1200	**97.87**	**0.00**	**0.00**	**2.13**
mn21h1200	91.65	5.60	0.00	2.75

The XRD patterns clearly show that there is reduction in sintering time by the use of oxygen atmosphere. The sintering time was reduced to 6 hours. But the expected decrease in secondary phase was not observed. The intensity (counts per second) of MN sintered at 1200° C in oxygen atmosphere was much high then that of MN sintered at 1100° C indicating smaller crystallite size. So the particle size will also be smaller than that of MN sintered at 1100° C. This may increase reaction rate for the synthesis of PMN due to the availability of larger surface area for reaction. The lowest amount of Nb_2O_5 was found in MN sintered for 6 hours and then in it started to increase gradually. While in case of $Mg_2Nb_6O_{11}$, there was constant reduction in the phase up to 12 hours and then it increases when sintered for 15 hours. Table 2 shows different phases formed during the sintering of MN in oxygen atmosphere in percentage.

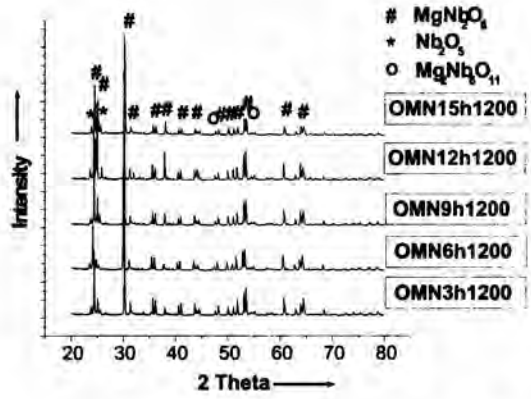

Fig. 6: Indexed XRD pattern of MN sintered at 1200° C up to 15 hours in flowing oxygen atmosphere.

TABLE 2: Different phases formed during the sintering of MN in oxygen atmosphere in percentage

Name	% of phases			
	$MgNb_2O_6$	Nb_2O_5	MgO	$Mg_2Nb_6O_{11}$
omn3h1100	90.20	6.38	0.00	3.42
omn3h1200	91.05	5.71	0.00	3.24
omn6h1200	91.06	5.88	0.00	3.06
omn9h1200	90.85	6.11	0.00	3.03
omn12h1200	90.52	6.63	0.00	2.85
omn15h1200	88.34	8.45	0.00	3.22

Now it is clear that use of oxygen reduces sintering time to a great extend, but the removal of secondary phases, as expected, does not takes place.

Hence MN sintered at 1200° C for 18 hours in air atmosphere was optimized for further synthesis, i.e. synthesis of PMN.

Lead Titanate (PT) was synthesized by heating a mixture of reactants PbO & MgO in stoichiometric proportions at 600° C and 700° C for 2 hours. XRD of these samples are shown in fig. 7.

It is clear from the graph that there is complete formation of PT sintered at 700° C for 2 hours. As the temperature increases, the amount of unreacted PbO and secondary phase $PbTi_3O_7$ decreases to zero. So sintering of PT is optimized at 700° C for 2 hours.

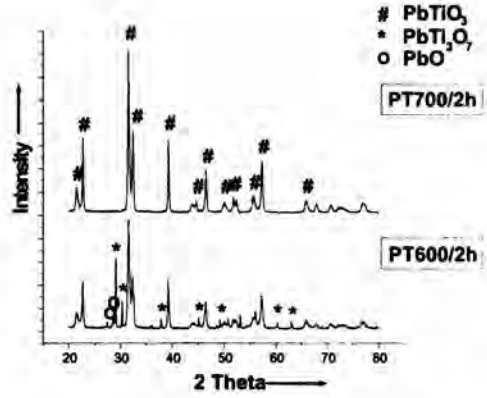

Fig. 7: XRD pattern of PT sintered at 600° C & 700° C for 2 hours.

PbO and PT were added to MN and sintered at 800° C for 3 hours to prepare 0.9PMN-0.1PT system. Since there is considerable loss of PbO above 800° C, PbO was added in excess by 6 and 8 mole percentages. Sintering was done in flowing oxygen atmosphere [12].The XRD patterns are shown in graph 8.

XRD pattern shows that the very sharp peaks of PMN are formed while that of PT could be hardly identified as the relative intensity is below 5%. Major phase was found to be Pervoskite along with pyrochlore phase. Table 3 shows different phases present in PMN-PT with 6 & 8 mole % excess PbO in percentage.

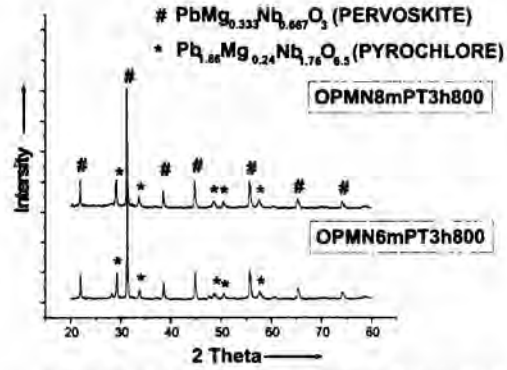

Fig. 8: XRD of PMN-PT sintered at 800° C for 3 hours in flowing oxygen atmosphere

Table 3: Different phases present in PMN-PT with 6 & 8 mole % excess PbO in percentage.

Name	% of Phases of PMN-pt	
	Pervoskite	Pyrochlore
opmn6mpt	81.43	18.57
opmn8mpt	84.60	15.40

The amount of Pervoskite phase in 8 mole % excess was found to be more then that of 6 mole % excess.

CONCLUSIONS

Synthesis of precursor MN in the oxygen atmosphere appreciably decreases the sintering time which is too long which sometimes extends upto 4 days [9-10]. Even calcination should be done in oxygen atmosphere so as to further decrease sintering time. PMN-PT should be synthesized at lower temperature in order to reduce or eliminate the PbO evaporation. Repetitive sintering may increase the pervoskite formation [11]. Sintering in oxygen atmosphere should be studied more extensively with different percentages of excess PbO additions to optimize sintering process.

ACKNOWLEDGEMENTS

I am thankful to Prof. T.R. R Mohan for his guidance and also to Deepak, Vikram, Rahul and all other labmates for their help.

REFERENCES

[1] G. A. Smolenskii and A. I. Agranovskaya, ***Sov. Tech. Phys.***, 3, 1380-82 (1958).

[2] G. A. Smolenskii and A. I. Agranovskaya, ***Sov. Phys. Solid State.***, 1, 1429 (1959).

[3] G. A. Smolenskii, V. A. Isupov and A. I. Agranovskaya, ***Sov. Phys. Solid State.***, 2, 2584 (1961).

[4] M Dambekale, A. Sternberg, I. Brante and M. Antonova, ***Ferroelectrics*** 69, 21 (1986).

[5] M Dambekale, I. Brante and A. Sternberg, ***Ferroelectrics***, 90, 1 (1989).

[6] S. L. Swartz and T. R. Shrout, ***Mat. Res. Bull.***, 17, 1245 (1982).

[7] E Goo, T. Yamamoto and K. Okazaki, ***J. Am. Ceram. Soc.*** 69, C-188 (1986).

[8] K. Okazaki, ***Am. Ceram. Soc. Bull.***, 67, 1946 (1988).

[9] K. Sreedhar and A. Mitra, ***Mat. Res. Bull.***, 32, 1643-1649 (1997).

[10] M. Dambekalne et al, ***Ferroelectrics***, 285, 259-264 (2003).

[11] S. M. Gupta and A. R. Kulkarni, ***Mat. Res. Bull.***, 28, 1295-1301 (1993).

[12] Seongtae Kwon et al, ***J. Am. Ceram. Soc***, 84, 3, 648-652 (2001)

STRENGTHENING BRASS POWDER COMPONENTS

Akhter H. Ansari

University Polytechnic, Aligarh Muslim University

Aligarh-202002, UP

ABSTRACT

It is difficult to manufacture brass powder components due to one of its constituents viz. zinc. Zinc is volatile and it evaporates during heat treatment (sintering). The vapors of zinc escape causing porosity in components. This affects the dimensions the components and adversely affects their mechanical properties. In the work under consideration, an attempt is made to produce powder components though a non-conventional route. In the present case, escaping vapors of zinc is tried to entrap by increasing the compaction pressure. An increase in compaction pressure increases the compressive strength of the (70:30) cartridge brass. The compressive strength of the components gets doubled by increasing the compressive pressure three times.

INTRODUCTION

The first attempt to produce brass powder metallurgy (P/M) parts was made in the United States and Britain in 1940s [1]. The production of brass parts from a mixture of copper and zinc powders by conventional powder metallurgy technique (pressing and sintering) presented considerable difficulties because zinc evaporated during sintering, and it was not possible to decrease the porosity of parts to less than 7 – 10%. This high residual porosity had a deleterious effect on the physico-machanical properties of materials. Apart from these, evaporation of zinc might have led to non-uniformity of chemical composition and hence physico-machanical properties across the specimens. The heterogeneity of P/M brass decreased markedly with the use of copper powders pre-alloyed with zinc [1]. The evaporation of zinc and the magnitude of volume shrinkage were observed to be closed and linearly related to each other [2]. As the quantity ^p/p (weight loss in sintering) grew, the level of strength of brass slightly fell, in particular by a factor of 1.5 at a fivefold increase in weight loss.

Re-pressing and repress-re-sintering had also shown improvements in mechanical properties. Repressing the parts had increased the strength of brass. It was also found to increase the density of the material to 7.9-8.1 g/cc. The operation reduced the elongation of the material of a sintered part from 15-17 to 8% [2-5]. The strength of P/M brass was increased by subjecting parts to coining, which had also increased their density to 7.9-8.1 g/cc. However, coining decreased ductility, from 5-7% to 2-3% for ordinary brass and from 13-15% to 8% for brass alloyed with phosphorus[2].

The percent theoretical values of density, hardness and compressive strength of brass filing swarf components obtained through DERH technique were found to be comparable with those obtained through muffle furnace heating (MFH) technique and these properties were superior for compacts made from atomized brass powder [6]. In an investigation it was observed that the current density affected the physical properties of atomized brass powder compacts [7]. Standard tensile test specimens' were produced from 80/20 (leaded) 70/30, 90/10 (non-leaded) and several other copper-base alloys at a pressure of 775 MPa[8]. Under different conditions, specimens' were sintered in partially covered graphite trays in dissociated ammonia for 30 minutes. It was observed that the mechanical properties increased with the zinc content.

Maximum strength characteristics (i.e. tensile strength σ_t=250-270 MPa and elongation $\in$ = 15%) were exhibited by brass alloyed with 0.3% P. An addition of 0.6% P decreased the tensile strength to 170 MPa, but increased the elongation to 17-18% [2]. Metallographic examinations had shown that raising the phosphorus content had increased the grain and that had accounted for the fall in strength. The strength and ductility of sintered brass were also reported to get increased when alloyed with small amount of red phosphorus (0.15-0.60 wt. %) [9]. Phosphorus was added in powder form (a ground copper-phosphorus or copper-zinc-phosphorus master alloy). The optimum amount was 0.3%. In that case the tensile strength was 250-270 MPa at an elongation of 15%. The addition of 0.6% of phosphorus decreased the tensile strength to 170 MPa while increasing the elongation to 17-18%. Metallographic

examinations had shown that the phosphide eutectic forming in sintered brass distributed itself along grain boundaries or formed separate inclusions. Humidity of an inactive atmosphere (nitrogen, hydrogen, dissociated ammonia, or endogas) also found to influence the evaporation of zinc. That should contain not more than 2% water vapor [10]. An increase of concentration of water vapour to 5% decreased the values of physico-machanical properties of brass by half [1]. That was due to oxidation of zinc during its evaporation. In view of the marked volatility of zinc, high rates of heating, cooling, and minimum duration of sintering were recommended [11]. A P/M brass composition had been patented containing 1-7% cobalt. The addition of cobalt to a charge had appreciably decreased sintering shrinkage and had increased the hardness and strength of sintered parts [12].

The pertinent literature survey shows a need to develop an economically viable simple sintering process for manufacturing brass products through P/M route. Since in most of the engineering applications strength of the component is a prerequisite, this property of a component is important. In the present work the effect of compaction pressure on the compressive strength of atomized brass powder components is explored.

Experimental conditions

Details of various parameters with relevant features used in the present investigations are provided in Table 1.

TABLE 1. Details of Parameters used in the present Investigation

Items	Parameters	Properties
Powder	Type	Pre-alloyed atomized brass powder
	Particle size	~100 μ m
	Chemical composition	Copper: 70.1% :: Zinc : 29.9%
	Apparent density	3.31 g/cc
	Flow rate	19.4 seconds/50 g
Component	Shape	Cylindrical
	Diameter	8.0 + 0.3 mm
	Thickness	10 mm – 13 mm
	Mass	3 g – 5 g
Variables	Compaction Pressure	242 MPa to 725 MPa

EXPERIMENTAL PROCEDURES

An electric current (d.c.) was passed axially through a powder component [13]. A predetermined current was maintained for a predetermined period. Likewise, 5 to 6 samples of components were treated for each set of predetermined experimental conditions. Standard deviation and mean were estimated for that experimental condition and used for analysis. Experiments were performed at three levels of compaction pressure.

RESULTS AND DISCUSSIONS

The heat treatment or sintering of powder compacts takes place in three phases. Initially, neck growth between particles develops rapidly, but powder particles retain their identity. In the second phase, the structure is recrystallized. However, the powder particles lose their separate identities and diffuse in to each other. Most of the densification occurs at this stage. In the third phase, isolated pores begin to spheroidize and densification progresses at a slower rate. The sintered parts exhibiting residual porosity possess poorer physico-mechanical properties compared to the similar parts produced by casting.

Strength of components

Figure 1 shows the effect of compaction pressure on the compressive strength of brass powder components. The compressive strength of components is about 15 MPa when the powder is compacted at a level of 242 MPa. Traces of zinc white are also observed on the surfaces of the components. This attributes evaporation of zinc and increase in porosity of the components. Evaporation of zinc in brass powder components was also observed in earlier investigations[13-16]. Some of these vapours of zinc may have segregated in the pores between the particles. Components undergoing second phase sintering may also depict low strength. Low compressive strength may be due to these phenomena.

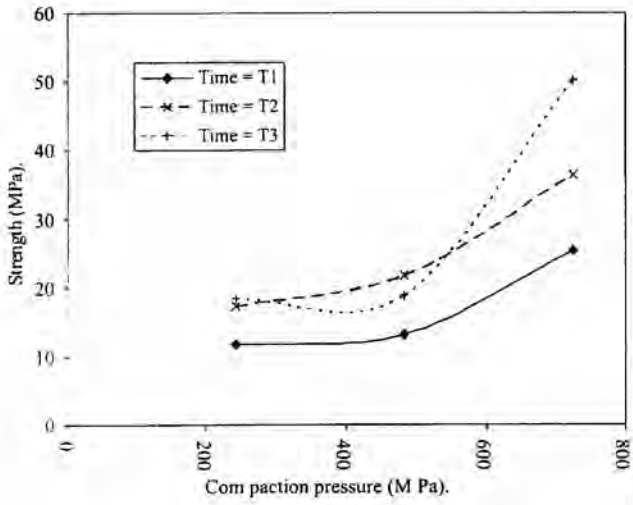

Fig. 1. Effect of compaction pressure on compressive strength of components.

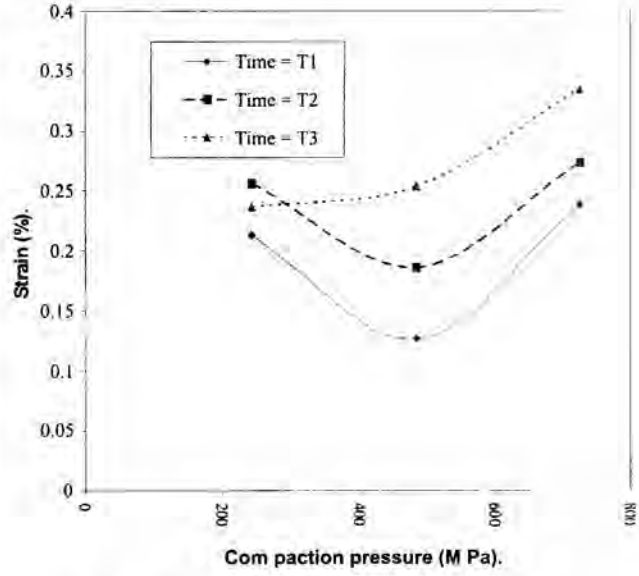

Fig. 2. Effect of compaction pressure on compressive strain of components.

An increase in compaction pressure is observed to increase in compressive strength. The increase in compressive strength attributes to fusion between the powder particles and strengthening inter-particle bonds. The increase in compaction pressure has reduced the pore size and the affinity for inter-particle fusion has increased. It also confirms the earlier findings[13] that the shrinkage of the components with an increase in compaction pressure is due to the fusion of powder particles at their boundaries. The increase in strength is more when the compaction pressure exceeds 483 MPa. The strength of the brass powder components is observed to be almost doubled when the compaction pressure is tripled.

Strain of components

Fig. 2 depicts the effect of compaction pressure on the compressive strain of brass powder components. The strain of the components after compacting them at 242 MPa is 0.23%. As discussed in the above paragraphs, the low strain confirms improper fusion between powder particles. An increase in the level of compaction pressure to 483 MPa has caused a little decrease in the strain. This is one more indication of second phase sintering which is in progress. A further increase in the level of compaction pressure has caused to increase the strain of the products. At 725 MPa, the strain has attained to a maximum of 0.35%. This attributes to an incomplete sintering.

CONCLUSIONS

Under this investigation, it can be concluded that compaction pressure affects the mechanical properties of brass powder components. An increase in the level of compaction pressure increases the affinity for inter-particle fusion. Inter-particle fusion is more significant at higher level of compaction pressure. The strength of components increases with an increase in the level of compaction pressure. The strain of brass powder components is low and it increases with an increase in the level of compaction pressure.

REFERENCES

1. A.V. Dovydenkova and I.D. Radomysel'skii, "Production and Properties of Constructional Parts from Copper and Copper Alloy Powders, A Review", Poroshk. Metall., No. 3, (1982) 44-53.

2. V.E. Terletskii, V.S Kalish, S.V. Bronin and V.A Shatskii, "Production of Brass Powder and Constructional Brass Parts", in: Sintered Constructional Materials, [in Russian], Inst. Probl. Materialoved., Akad.Nauk Ukr. SSR, Kiev pp.17-25, 1972.

3. W. Cegielski, "Investigation of the Brass Powder Atomization Process", Prace Inst. Met. Niezelaznych, Vol. 7, No. 3, pp. 139-143, 1978.

4. V.E. Terletskii, I.Yu. Epshtein and S.V. Bronin, "Production of Sintered Brass from Unhomogenized Powder Mixtures by Liquid-Phase Sintering", in: Sintered Constructional Materials, [in Russian], Inst.

Probl. Materialoved., Akad.Nauk Ukr. SSR, Kiev pp. 51-55, 1976.

5. P. Groat, "Manufacture of Parts from Iron Powder" [Russian Translation], Mashgiz, Moscow, 1960.

6. A. Afaq, and M. Hameedullah, "Potential of DERH technique in sintering the brass filing swarf compacts", Advances in Powder Metallurgy and particulate materials - 1995, v. 1, pt. 4, pp. 163-173, 1995.

7. A. H Ansari, M. Hameedullah and A. Afaq, Advances in powder metallurgy and particulate materials, MPIF, 1 part 4 (1995) 153 – 161.

8. P. Mathews, "The mechanical properties of brass and developmental non-ferrous P/M materials", Int. J. of Powder Metallurgy, v. 5, n. 4, pp. 59-69, 1969.

9. G.T. Brown and R.R. Jones, "Experimental Aspects of the Powder Forging Process", Modern Development in Powder Metallurgy, Vol. 4, New York, pp. 369-371, 1971.

10. J. Willcock and R.J Woolfall, "Pressing and Sintering of Nickel Brasses", Metallurgiya, Vol. 63, No. 4, pp. 378-382, 1979.

11. E. Paller and D.A. Grimme, "Investigation of the Possibility of Producing Sintered Brass Parts", [in Russian], New Materials Produced by the Powder Metallurgy Method, Moscow, pp. 137-146, 1966.

12. U.S.A. Pat. No. 4139378, "Sintered Cobalt-Containing Brasses", 1979.

13. A.H. Ansari, M. Hameedullah and M.S.J. Asghar, "Stabilising dimensions of brass powder components", Indian Journal of Engineering & Materials Sciences, Vol. 11, December, 2004.

14. A.H. Ansari, M. Hameedullah and M.S.J. Asghar, "Dimensional behavior of P/M brass products", Presented in 29th National P/M Conference, PMAI, Goa, January 30-31, 2003.

15. A.H. Ansari, "Density retention of P/M component during its processing", Presented in 30th National P/M Conference, PMAI, Kolkata, January 30-31, 2003.

16. A.H. Ansari, "Study of microstructure of Powder Metallurgy brass components", Presented in 30th National P/M Conference, PMAI, Kolkata, January 30-31, 2003.

Polymethylmethacrylate / Hydroxyapatite Composites

Rajalaxmi Dash, Deepak K. Pattanayak, B. T. Rao, R. C. Prasad and T. R. Rama Mohan

Dept. of Metallurgical Engineering and Materials Science Indian Institute of Technology, Bombay Powai, Mumbai - 400076

ABSTRACT

Bioglasses and various types of glass ceramics (Hydroxyapatite / apatite wollastonite / ceravital) are used as bone or dental filling ceramics. These can integrate with bone and form apatite layer on the surface which helps in anchoring with the surrounding tissues in the human body. However, the brittleness of these ceramics restricts their use as a load bearing implant. In order to improve the strength of bioceramics attempts are made to develop composites using various bioactive polymers or metals in combination with the ceramics.

In the present study, bioactive composite was prepared using hydroxyapatite and polymethylmethacrylate (PMMA). Samples of various proportions (10, 20, 30, 40 and 50 by wt %) of PMMA in HA ceramics were prepared by hot press at 150°C and 250 MPa pressure. Biaxial flexural strength (BFS) of the composites was measured and the fractured surfaces were analyzed in environmental scanning electron microscope (ESEM). BFS of 23 MPa was obtained for 20 wt % PMMA composites and then the strength was found to decrease with increase in PMMA. In vitro bioactivity of the composites was studied by soaking the composites in simulated body fluid (SBF) for 7, 14 and 21 days. Phosphate like growth was observed by ESEM just after 7 days of soaking in SBF and the EDAX analysis confirmed the increase in Ca and P content on the sample surface with increase in soaking period.

INTRODUCTION

The development of load bearing and bioactive implant has raised the increasing interest in fundamental research on biomaterials over past few decades. A lot of attempt has been made to design an implant using various materials like metals, ceramics and polymers. But there are certain advantages and disadvantages of these materials. Metallic implants though providing superior mechanical strength as compared to other materials, they induce the stress shielding with the surrounding bone tissues [1]. This stress shielding or stress protection arises from the mismatch of stiffness between the bone and implant. As a result loosening of the implant occurs and hence prevents the healing process. Another point is the biocompatibility of the metals. When they are used as a monolithic material, they hardly bind to the living tissue. However, at the same time there are some bioactive ceramics like hydroxyapatite (HA), bioglasses, apatite wollastonite which have wide applications in the medical field are found to be biocompatible as well as osteoconductive [2-4]. So they strongly integrate with the bone. But their application is limited because of their low strength. Depending on the application and use the polymers like polyethylene, polyetherketone, polylactic acid etc. [5-9] are used because of their wide availability in composition and properties. However, they are too weak to meet the mechanical properties of most applications. So all these things demand the development of a bioactive composite [10,11] system with good mechanical and biological properties for potential application. The advantage of composite materials over monolithic is by controlling the volume fraction of the reinforcement phase, the properties and design of an implant can be varied and tailored to suit the mechanical and physiological conditions of the host tissues.

In the present study, composites were prepared using hydroxyapatite and polymethylmethacrylate (PMMA) powder by hot pressing the mixture of two in different proportions. Biaxial flexural strength was measured and fractured surfaces were analyzed by ESEM. In vitro assessment was done by soaking the samples in simulated body fluid for different durations and the sample surfaces were characterized by ESEM, EDAX, and FTIR and the results were compared with un soaked composites.

EXPERIMENTAL

Preparation of hydroxyapaptite powder

Hydroxyapatite powder was prepared by precipitation method. Di-hydrogen ammonium phosphate dissolved in distilled water was mixed with the calcium nitrate solution slowly by constant stirring, with the help of a mechanical stirrer. The pH of the solution was maintained in between 11-12. After mixing the solution, it was left for 24 hours with constant stirring. Then the precipitate was decanted, filtered and dried in an oven at 100°C for 15-16 hours. The dried hard mass was crushed and ball milled for two hours to form the HA powder. Based on the preliminary results the powder was calcined at 400°C and was used for composite preparation.

Preparation of composites

Polymethylmethacrylate (MW. 1,50,000) granules were made into powder with the help of a mixer. In order to obtain a homogeneous mixture, both HA and PMMA powders were mixed in a ball mill for two hours. Small amount of polyethylene glycol was added to the mixed powder to improve the plasticity of the composites. Cylindrical composites of 15 mm diameter were prepared by hot pressing the composite powder at about 150°C and 250 MPa pressure. The preparation procedure in the form of a flow diagram is shown in Figure 1. Various compositions of samples were made by replacing 10, 20, 30, 40 and 50 weight fraction of HA in PMMA powder.

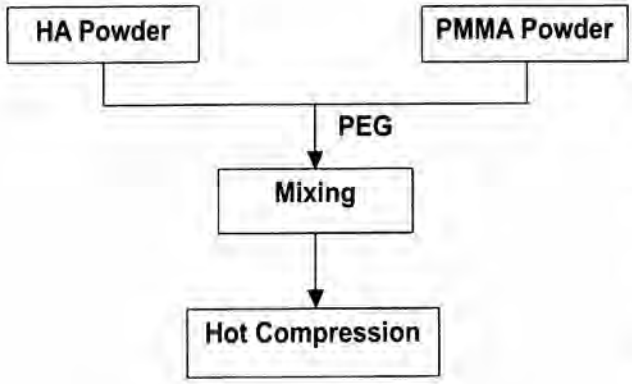

Figure 1: Flow diagram for the preparation of PMMA / HA composites.

Preparation of simulated body fluid (SBF)

SBF is known to be a meta-stable buffer solution and even a small, undesired variance in both the preparation steps and storage temperatures, may drastically affect the phase purity and the stability of the desired material. SBF was prepared by dissolving appropriate quantities of NaCl (99.5%), $NaHCO_3$ (99.5%), KCl (99%), $Na_2HPO_4.2H_2O$, $MgCl_2.6H_2O$ (99%), Na_2SO_4, $(CH_2OH)_3CNH_2$ (99.5%), $CaCl_2.H_2O$ (99%) in de-ionized water. Reagents were added, one by one after each reagent completely dissolved in 700 ml of de-ionized water. 15 ml of 1 M HCl was added before the addition of $CaCl_2.H_2O$. Otherwise the solution will show slight turbidity. The remaining part of HCl was used in subsequent titration. After addition of the last reagent the solution was titrated with 1 M HCl to maintain a pH of 7.4. During the titration process, the solution was also continuously diluted with the de-ionized water to make the final volume 1 liter. In vitro bioactivity of the composites was studied by soaking the samples in SBF.

Characterization

XRD patterns of the composites, soaked samples as well as HA and PMMA were recorded using Philips PANalytical instrument (Cu Kα radiation) in the range of 20-80. The characteristic peaks and their intensities were compared with the standard ICDD file. BFS of the composites was measured by a servo hydraulic universal testing machine (UTM) until the failure takes place. The test was carried out for five samples of each composition. The load from the graph was taken in order to calculate the BFS by using the equation

$$S = -0.2387\ P\ (X-Y) / d^2$$

Where, S = Flexural strength in MPa and P is the breaking load (N).

$$X = (1+\upsilon)\ \ln (B/C)^2 + [(1-\upsilon)/2]\ (B/C)^2$$

$$Y = (1+\upsilon)\ [1+\ln (A/C)^2] + (1-\upsilon)\ (A/C)^2$$

υ is the Poisson's ratio and is assumed to be 0.25.

A is the radius of the supporting circle in mm, B the radius of ram tip in mm, C the radius of specimen and d is the thickness of the sample.

Fracture surfaces as well as surface morphology of the composites before and after soaking were studied in the environmental scanning electron microscope (Quanta 200). FTIR analyses were made on a Nicolet Magna IR 550 spectrophotometer in the scanning range of 400 – 4000 cm^{-1}. Analysis was performed in absorbance mode in order to characterize the formation of calcium phosphate layer on the surface. The change in concentration of the elements on the sample surface was determined by energy dispersive X-ray analysis (EDAX).

DISCUSSIONS

Figure 2 (a) – (g) shows the XRD pattern of PMMA, prepared HA powder and the composites containing various amounts of PMMA in HA. Figure 2 (a) showed a broad peak which indicated the amorphous nature of the polymer (PMMA) used.

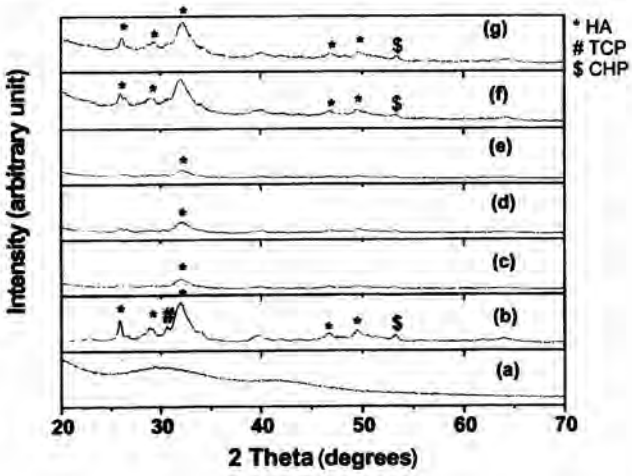

Figure 2: XRD of (a) PMMA (b) HA (c) 10 (d) 20 (e) 30 (f) 40 and (g) 50 weight percent of PMMA composites.

XRD spectrum of prepared HA powder calcined at 400°C and pressed at 150 °C is shown in Figure 2 (b). HA along with other minor phases like tricalcium phosphate (TCP), calcium hydrogen phosphate (CHP) was observed and the powder contained some amount of glassy matrix as the spectra did not show any well crystalline peaks. Figure 2 (c)-(g) showed the HA lines corresponding to their d values irrespective of PMMA content.

Density and biaxial flexural strength

Figure 3 (a) and (b) shows density and biaxial flexural strength of the composites with varying percentages of PMMA. 20 wt % PMMA compositions showed maximum density and then it decreased with increase in PMMA. This could be due to the low density of PMMA used. BFS was found to increase from 19 MPa to 23 MPa when PMMA content increased from 10 to 20 wt %. Above 20 wt% a steady decrease in the flexural strength was observed. The low value of the flexural strength may be due to the poor adhesion between the polymer and ceramic particles. Thus a proper mixing takes place up to 20 wt % PMMA. Beyond which the mixing was not uniform which can be concluded from Figure 3 (a). Thus 20 wt % PMMA can be incorporated in HA matrix to achieve the maximum strength.

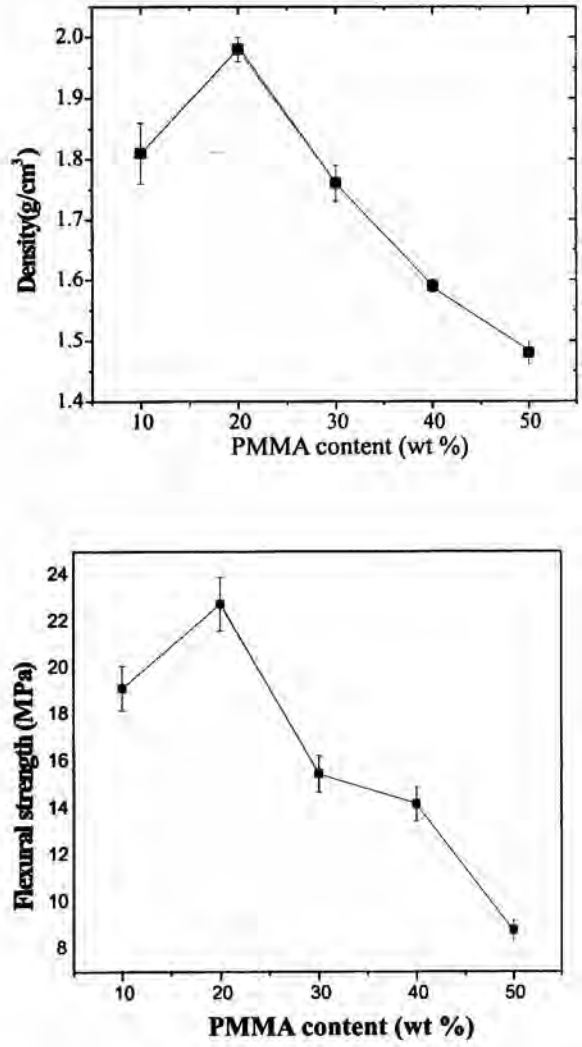

Figure 3: Variation in (a) density (b) biaxial flexural strength with PMMA content.

Fractography

Fracture surfaces of the composites containing varying percentages of PMMA were observed in an Environmental scanning electron microscope and is shown in Figure 4 (a-e). For most brittle materials, crack propagation takes place in successive and repeated breaking of atomic bonds along some specific crystallographic planes. The fracture surface of 20 wt % PMMA composites, shown in Figure 4(b) is macroscopically rough than that of the other compositions indicating rapid crack propagation and considerable crack branching. With increase in the PMMA content the voids were found to increase and these voids might be responsible for the lower biaxial flexural strength of the composites.

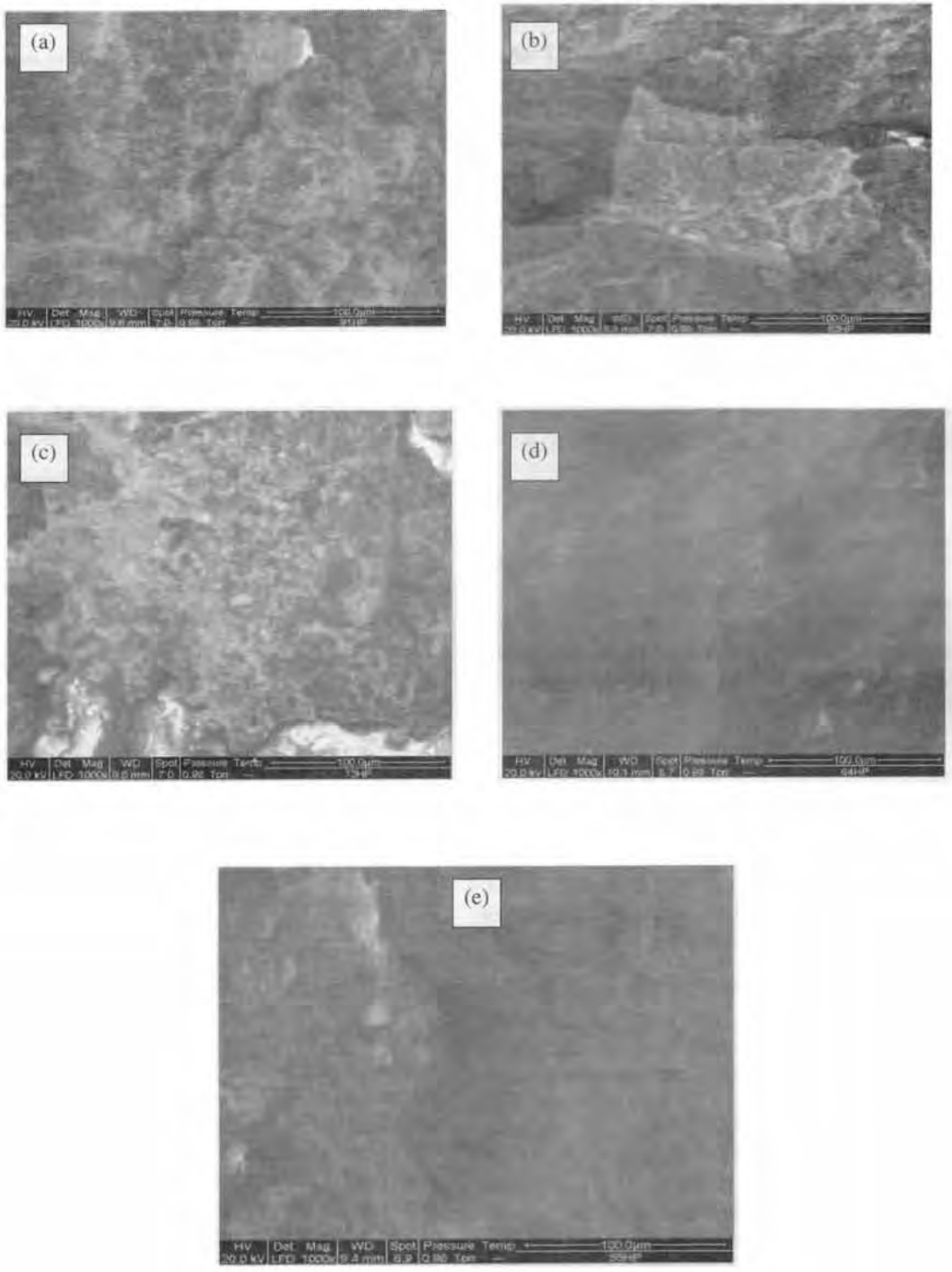

Figure 4: ESEM of the fracture surfaces of (a) 10 (b) 20 (c) 30 (d) 40 and (e) 50 weight percent of PMMA / HA composites X 1000.

In vitro bioactivity study

In vitro bioactivity of the composites containing 20 wt % PMMA was carried out by soaking the samples in SBF for 7, 14 and 21 days. The morphology of the sample surfaces before and after soaking in the SBF is shown in Figure 5 (a-d). In Figure 5 (a) HA particles were found to be distributed in PMMA. However, precipitation of phosphates in the form of globules were observed just after 7 days of soaking in SBF which is shown in Figure 5 (b) and the growth of phosphate layer was found to increase with increase in soaking period (c and d).

Dispersed HA particles as well as surface porosities present in the composites would have acted as the site of nucleation of these phosphate globules during soaking. Further the growth of the globules increased with the increase in soaking period and the precipitation of these phosphates were from SBF and in turn it increased the calcium and phosphorous content on the SBF studied samples that are observed by EDAX.

Energy dispersive X-ray analysis

In order to see the compositional change of the sample surface during soaking EDAX was carried out. The relative weight percent of calcium and phosphorous obtained from the EDAX of the sample surface before and after soaking in SBF is shown in Figure 6. The relative weight percent was calculated by using the equation $[(W-W_0) / W \times 100]$.

Where W represents the weight percent of the elements on the sample surface before soaking and W_0 represents weight percent of the elements after soaking. It indicated that both calcium and phosphorous ions moved from the solution to the sample surface and precipitated.

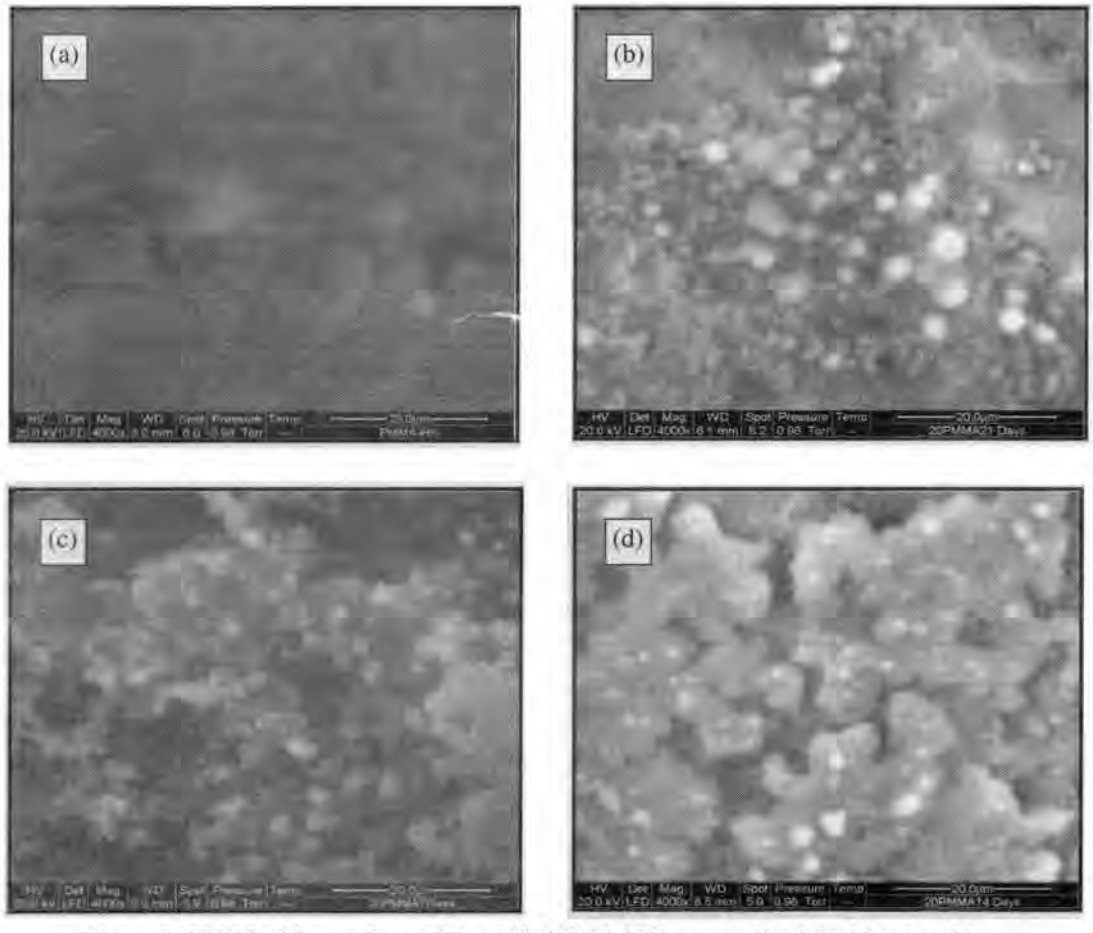

Figure 5: ESEM of the surfaces of 20 wt % PMMA / HA composites (a) without soaking (b) 7 (c) 14 and (d) 21 days soaking in SBF X 4000.

Fourier transform infrared spectroscopy

Development of the apatite (phosphate) layer was observed using FTIR spectroscopy after mixing the powders scratched from the surface of the samples with KBr (1:50 by wt.). Figure 7 shows the FTIR of the samples without soaking and after 21 days of soaking in SBF. A strong peak at 1035 cm^{-1} corresponds to the PO_4^{3-} group. The broad band at 3424 cm^{-1} is due to the –OH vibrational mode. Very weak peak at 1731 cm^{-1} can be attributed to the carbonyl C=O group of polymethylmethacrylate. The peaks at 558 and 603 cm^{-1} were due to P-O stretching modes. It was found that the absorbance of all these functional groups increased after soaking in SBF. This can be attributed to the formation of more and more calcium and phosphate layers on the surface of the sample.

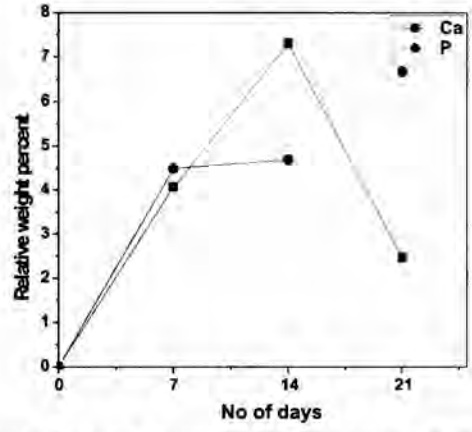

Figure 6: Relative weight percent of elements of 20 wt% PMMA / HA samples as obtained from EDAX

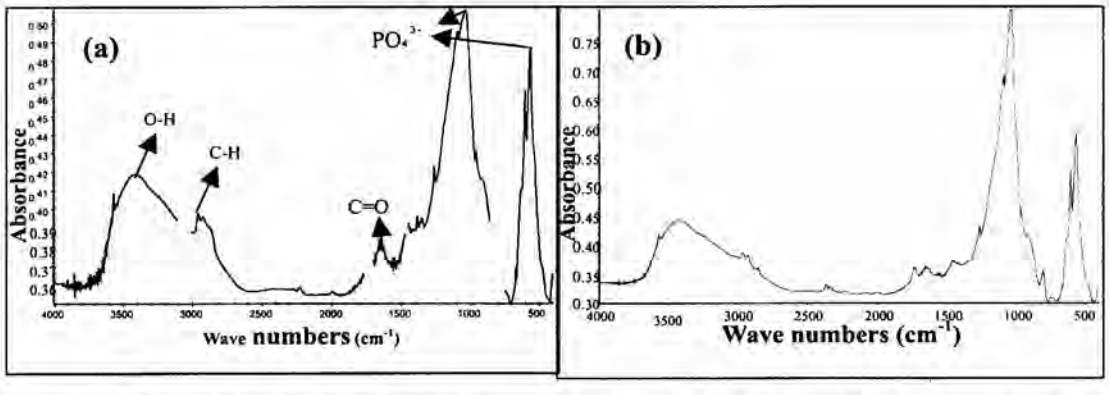

Figure 7: FTIR spectra of the 20 wt % PMMA / HA composites (a) without soaking (b) 21 days soaking in SBF.

CONCLUSIONS

Composites containing up to 50 wt % PMMA could be prepared by hot press. Biaxial flexural strength of (23 MPa) was obtained for composites containing 20 wt % PMMA and the strength decreased with increase in PMMA content. In vitro bioactivity studies showed the growth of calcium phosphate layer on the sample surface just after 7 days of soaking in SBF. From EDAX analysis it was found that calcium and phosphorous was exchanged from simulated body fluid to the sample surface. The presence of PO_4^{3-},

OH groups on the sample surface after soaking was confirmed by the FTIR results.

REFERENCES

1. S. Ramakrisna, J. Mayer, E. Wintermantel and K. W. Leong, "Biomedical application of polymer composite materials: a review", Composites Science and Technology, **61**, 1189-1224, (2001).

2. M. Wang, "Developing bioactive composite materials for tissue replacement", Biomaterials, **24**, 2133–2151, (2003).

3. R. M. Pilliar, M. J. Filiaggi, J. D. Wells, M. D. Grynpas and R. A. Kandel, "Porous calcium polyphosphate scaffolds for bone substitute applications-in vitro characterization", Biomaterials, **22** (9), 963-972, (2001).

4. H. Y. Yasuda, S. Mahara, Y. Umakoshi, S. Imazato and S. Ebisu, "Microstructure and mechanical property of synthesized hydroxyapatite prepared by colloidal process", Biomaterials, 21 (20) , 2045-2049, (2000).

5. W. Bonfield, M. D. Grynpas, A.E. Tully, J. Bowman, and J. Abram, "Hydroxyapatite reinforced polyethylyne a mechanically compatible implant material for bone replacement", Biomaterials, **2**, 185–186, (1981).

6. D.K. Pattanayak, D. Srivastava, R. Iyer, B. T. Rao and T.R. Rama Mohan, "Bioactive Sodium-Bioglass / Polythene Composites" J. Am. Ceram. Soc., **88** (9), 2655-2658, (2005).

7. S.M. Zhang, J. Liu, W. Zhou, L. Cheng, and X.D. Guo, "Interfacial fabrication and property of hydroxyapatite / polylactide resorbable bone fixation composites," Current Applied Physics, **5** (5), 516-518, (2005).

8. S. Yu, K. P. Hariram, R. Kumar, P. Cheang and K. K. Aik, "In vitro apatite formation and its growth kinetics on hydroxyapatite/ polyetheretherketone biocomposites", Biomaterial,, **26**, 2343–2352, (2005).

9. R. Zhang and P. X. Ma. "Porous poly (L-lactic acid /apatite composites created by biomimitic process", J. of Biomedical Materials Search, **45** (4), 285-293, (1999).

10. G. Pezzotti and S. M. F. Asmus, "Fracture behavior of hydroxyapatite / polymer interpenetrating network composites prepared by in situ polymerization process ", Materials Science and Engineering A, **316** (1-2) , 231-237,(2001).

11. K. Katti and P. Gujjula "Mechanical responses in insitu polymer-hydroxyapatite composites for bone replacement", 15th ASCE Engineering mechanics conference, June 2-5, (2002). Columbia University, New York.

NANOSTRUCTURED IRON POWDER BY CARBOTHERMIC REDUCTION OF MECHANICALLY ACTIVATED MILL SCALE

Manoj Dubey*, Ashish Bhatnagar*, N. Charles*, Nilima Lodha, P.R. Soni***

*Department of Metallurgical Engineering Malaviya National Institute of Technology Jaipur - 302017 ***,

**Department of Physics, University of Rajasthan, Jaipur-302017

ABSTRACT

Mill scale is abundantly available as by-product of steel rolling mill operations, which is basically an iron oxide of the approximate composition Fe_3O_4. Mechanical activation of the mill scale has been carried out by milling it in a high energy attrition mill for 60 hours. The activated mill scale was then carbothermally reduced at lower temperature of 950°C. This enhanced reduction mainly results from the intimate mixing and large contract area between milled mill scale and carbon particles. The resultant powder was characterized for its size, shape, flow rate, apparent density and compressibility.

INTRODUCTION

The past decade has seen significant advances in the synthesis and processing of materials at the nanometer scale [1,2]. The techniques used for the production of micrometer scale powders fail in the sub micrometer range. Methods such as gas or water atomization have a lower size limit of about 1-5 μm. Milling is used for particle size reduction of very brittle materials like ceramics or hard metals but it generally fails for ductile materials, such as precious metals, copper, and aluminum [3]. However, a variety of methods are available for the production of ultra fine powders with sub micrometer particle size. Gas phase reactions, spray drying, and precipitation methods are used most frequently. Other methods such as flame reduction or plasma reduction use the decomposition and reduction of metal salts in a gas flame or plasma. Using commercial coarse-grained metallic powders as the starting material, mechanical milling produces the nano grained microstructure through the introduction of dislocations during the severe mechanical deformation [4]. Mechanical milling is attractive for potential commercial applications because the technique is simple and inexpensive route that is performed at room temperature, and straightforward to scale up for mass production [5,6]. The main problems in production and processing of nanopowders are caused by the small particle size and the corresponding high specific surface area. As for main quality-issue, the pick-up of oxides or nitrides during processing or storage must be prevented. As nanopowders are often used or processed in suspension, the degree of agglomeration is also a quality-issue due to the need for de-agglomeration of the powders. Nanoscale powders are finding potential applications in polymer composites for microelectronics[3,7], hydrogen storage [8], metal bonding applications [3] and in metal injection moldings(MIM) [9,10].

Mechanical milling can also be used effectively to decrease the T_{crit} and concomitant increase in reduction rate [11]. The process has been applied to reduce a number of metal oxides [12] and halides [13] to pure metals.

In the last few years, a rapid increase in the cost of engineering materials followed by an increase in the cost of energy has drawn attention of many researchers to find a suitable method for more economical reclamation of metallic scrap generated in the different industries. Mill scale is abundantly available as by- product of steel rolling mill operations which is basically an iron oxide of the approximate composition Fe_3O_4. The aim of the present work is to study the effect of mechanical milling of the mill scale on activation of the carbothermic reduction reaction and to characterize the iron powder produced.

EXPERIMENTAL

The mill scale used in these investigations was procured from local industry. After separating dust, dirt and non-magnetic impurities using magnetic separator, the mill scale was screened to -100 mesh (<149μm). Philips X'Pert-Pro X-rays Diffractometer was used to analyze the types of oxides present in the raw material .The iron percentage in the mill scale was analyzed using wet analysis. For mechanical activation the mill scale and activated carbon powder were mixed in 5.7 : 1 ratio and milled in laboratory attrition mill, having mill chamber and impellers made of stainless steel, under the following parameters : RPM – 330, grinding ball (hardened steel) dia = 8 mm, ball to charge ratio –10:1. Milling was carried out on three samples in air atmosphere for different time intervals of 20hrs, 40 hrs and 60 hrs, respectively.

For reduction, four samples viz. mixed powders, and 20 hrs, 40 hrs and 60 hrs milled powders were tightly sealed

in ceramic tubes. These sealed tubes were then put in an electrical furnace for reduction at 950°C for 24 hrs. The sponge iron powder produced was pulverized and cleaned magnetically.

X-rays diffraction (XRD) patterns of unmilled, milled and of the reduced powders were taken using the diffractometer, with iron target (λ = 1.94 Å). Optical micrograph of cross-section of the reduced iron powder was taken.

RESULTS AND DISCUSSION

The types of oxides present in the mill scale are given in Table 1.. By wet analysis the mill scale was found to contain 71% of Fe.

XRD – pattern of umilled and milled samples shown in Figure 1 (a-d) indicates that reduction does not starts during milling up to 40 hrs of milling. However, the reduced iron was detected in 60 hrs milled sample (fig.1.d). The average size of the crystallite in these samples was estimated from diffraction peak broadening using Scherrer's formula ($d = .9\lambda / B \sin\theta$) [13], and shown in Figure 2 as a function of milling time.

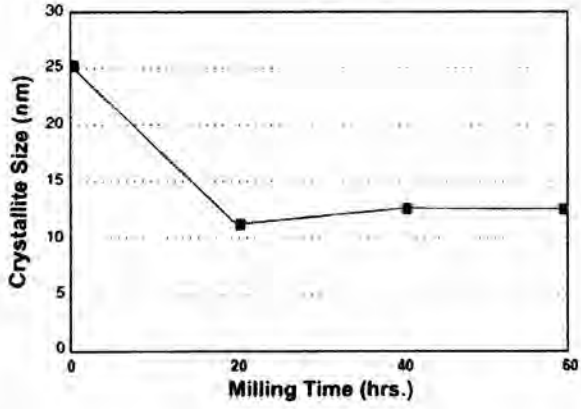

Fig.2 Size reduction of the mill scale crystallite as a function of the milling time.

TABLE I : Constituents of the mill scale at different milling times

Sample No.	Milling time (hrs.)	Constituents			
		Magnetite (Fe_3O_4) (%)	Hematite (Fe_2O_3) (%)	Westite/Pestite ($Fe_{1-x}O_x$) (%)	Iron (Fe) (%)
1.	0	58	32	10	—
2.	20	70.7	24.2	05.1	—
3.	40	75	25	—	—
4.	60	70	25	—	05

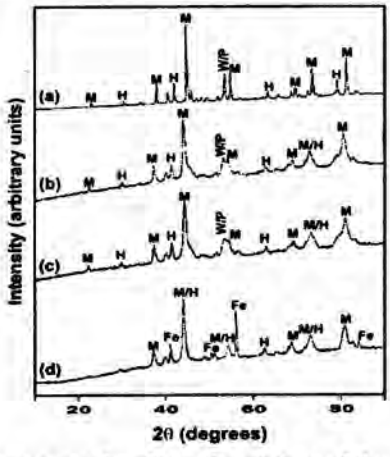

Fig. 1 XRD patterns taken from the mixture of the mill scale and the activated carbon milled for different time period (a) 0 hrs. (b) 20 hrs. (c) 40 hrs. and (d) 60 hrs. M : Magnetite (Fe_3O_4), H : Hematite (Fe_2O_3), W : westite ($Fe_{0.95}O_{0.05}$) , P : Pestite

By wet analysis, it was revealed that reduction in the cases of mixed sample, 20 hrs, 40 hrs and 60 hrs milled samples took place to the extend of 12%, 24%, 95%, and 100% respectively. The progressive increase in percentage of reduction indicates progressive increase in surface activation with milling hours, which is slow initially but increases rapidly with milling hours (Figure 3). This increase in surface activation results in reduction reaction possible at lower temperature 950°C (normally such reduction reaction takes at 1250°C) and a higher reduction rate. The enhanced reduction reaction induced by milling mainly results from the intimate mixing and large contact area between milled mill scale and carbon particles. Figure 4 show XRD – pattern of iron powder produced by reduction of 60 hrs milled mill scale. The Scherrer's calculation gives an average crystallite size of 25 nm in the powder.

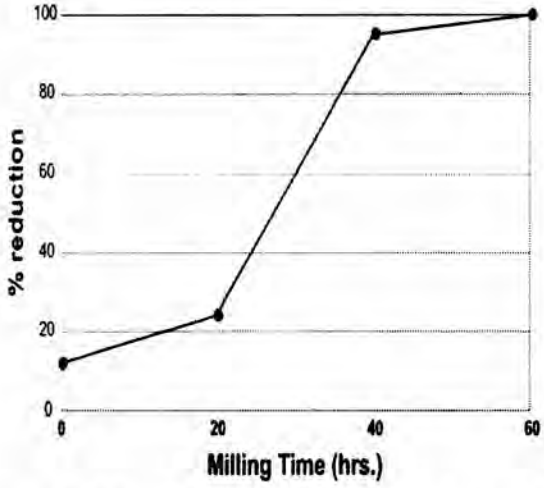

Fig.3 Percent reduction of mill scale as a function of the milling time.

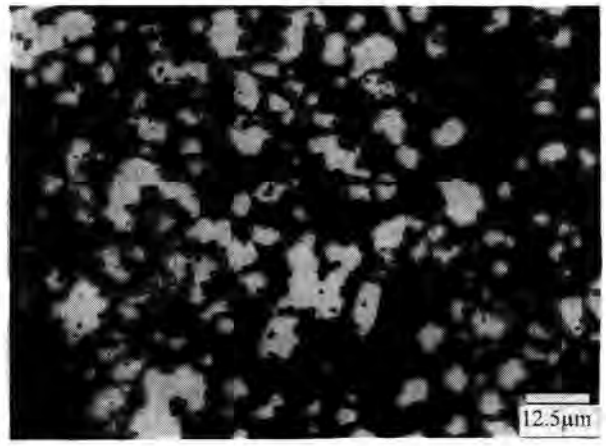

Fig. 5 Optical micrograph of cross section of reduced iron powder.

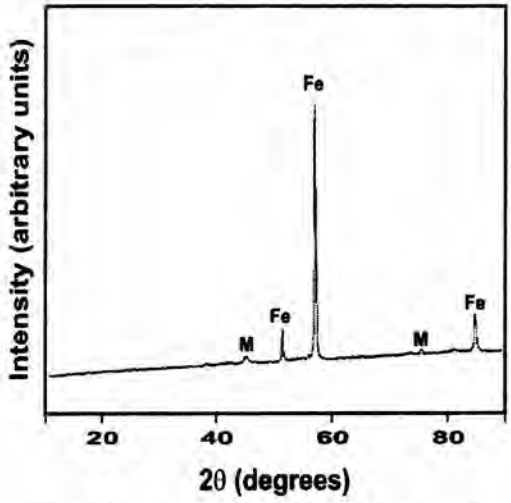

Fig.4 XRD pattern taken from the reduced iron powder produced by carbothermic reduction of mill scale.

Figure 5 shows optical micrograph of cross-section of the reduced iron powder. The pores in the interior structure of the powder particles are considerably less and finer than those present in Swedish sponge iron powder and Pyron iron powder due to enhanced reduction reaction at lower temperature. Because of the finer pore structure, the powder have high apparent density of 3.12 g/cm^3 (Table II), and compacts of this powder may sinter faster

The iron powder produced was subjected to detailed characterization and the results are summarized in the Table II.

TABLE II

Properties of iron powder produced by carbothermic reduction of mill scale

Characteristic	Value obtained
Apparent density	3.12 g/cm^3
Flow rate	Non-free flowing
Compressibility*	6.52 g/cm^3
Chemical analysis	
Carbon	.005%
Sulphur	.005%
Phosphorus	.001%
Acid insoluble	0.3%
H_2 loss	1%

*at 600 MPa, without powder lubrication

CONCLUSIONS

(i) Attrition milling of the mill scale results in intimate mixing and surface activation which enhances reduction rate and decreases reduction temperature in carbothermic reaction.

(ii) Milling decreases average particle size in the mill scale which provides sponge iron powder of fine size after reduction.

ACKNOWLEDGEMENTS

Authors are thankful to Dr. Anwar Raish and Dr. Goutam Mukhophodhyay of GSI, WR, Jaipur for their cooperation in X-rays diffraction analysis of the mill scale and milled powders.

REFERENCES

1. B.H. Kear and Ganesh Skandan, "Overview : Status and Current Develcpments in Nanomaterials", The International Journal of Powder Metallurgy, Vol. 35, No. 7, PP 36-37 (1999).

2. B. Gunther, Met. Powder Rep, Vol. 26, No. 2, PP 30–36 (1995).

3. H. Eifert, D. Kupp and B. Gunther, "Production Methods and Applications of Low Impurity Metal Nanopowders", Powder Metallurgy, V.43, No. 4, P P.310-313 (2000).

4. P.R. Soni, Mechanical Alloying : Fundamentals and Applications, Cambridge International Science Publishing, UK, PP. 40-51 (2000).

5. E. Ma, "Consolidation and Mechanical Behaviour of Nanophase Iron Alloy Powders by Mechanical Alloying", Ibid reference 3, PP. 306-310.

6. Y. Kimura and S. Takaki, "Ultra Grain Refinement of Iron by Mechanical Milling" Powder Metallurgy, Vol. 46, No. 12, PP 1235-1241 (1999).

7. G. Skandan and A. Singhal, " Tailoring Nanostructured Powders for Functional and Structural Applications", Ibid reference 3, PP. 313-317.

8. M.L. Trudean and R. Schultz, "High-resolution electron microscopy study of Ni-Mo nanocrystal prepared by high-energy mechanical alloying" Materials Sci. and Eng., V. 134 A, PP. 1361 (1991).

9. J.C. Kim, S. S. Ryu, H. Lee and I. H. Moon, " Metal Injection Molding of Nanostructured W-Cu Composite Powder" The International Journal of Powder Metallurgy, Vol. 35, No. 4. PP 47-55 (1999).

10. J. Fan, B. Huang, X. Qu and K. A. Khalil, "MIM of Mechanically Alloyed Nanoscale W-Ni-Fe Powder", The International Journal of Powder Metallurgy, Vol. 35, No. 6, PP 56-61 (2002)

11. Ibid reference 4, PP. 51-53.

12. Y. Chen, T. Hwang, M. Marsh and J.S. Williams, " Mechanically Activated Carbothermic Reduction of Ilmenite," Mat. and Mater. Trans, V. 28 A, No. 5, PP 1115-1121 (1997).

13. R. Ricceri and O. Matteazzi, " Mechanicochemical Synthesis of Elemental Boron", The International Journal of Powder Metallurgy, Vol. 39, No. 3, PP. 48-52 (2003).

14. B.D. Cullity, Elements of X-ray diffraction, Adison-wesley, London, P.P 81–106 (1978).